Geothermics 142 (2026) 103788

Contents lists available at ScienceDirect

Geothermics

journal homepage: www.elsevier.com/locate/geothermics

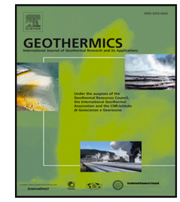

Uncertainty quantification under data worth for the Delft campus geothermal project

Yuan Chen [a,*], Guillaume Rongier [a], James Robert Mullins [c], Denis Voskov [a,b], Alexandros Daniilidis [a]

[a] Department of Geoscience & Engineering, TU Delft, Stevinweg 1, 2628 CN Delft, The Netherlands
[b] Department of Energy Science & Engineering, Stanford University, Stanford, CA 94305, USA
[c] GeoIQ, 4 Rubislaw Terrace, Aberdeen, AB10 1XE, United Kingdom

ARTICLE INFO

Keywords:
Geothermal doublet
Direct-use heating
Uncertainty quantification
Numerical simulation
Sensitivity analysis
Data worth

ABSTRACT

Low-enthalpy geothermal doublets for direct-use heating are highly sensitive to subsurface heterogeneity and operational uncertainty. This study quantifies these uncertainties for the Delft campus geothermal system using an integrated workflow that couples geological modeling with GPU-accelerated, high-spatial-resolution reservoir simulation. Ensembles of three-dimensional regional-scale facies models of the Delft Sandstone Member, with and without conditioning to Geothermie Delft (GTD) well data, were generated using object-based modeling and sequential indicator simulation. Porosity was modeled by sequential Gaussian simulation, and permeability was derived from a nuclear magnetic resonance-based porosity–permeability correlation calibrated to GTD well data, yielding higher permeability than core-based correlations for porosity below 15%. Lorenz coefficients indicate strong variability in property distributions, resulting in a wide spread of production temperatures. In total, 2000 geological realizations were simulated over 50 years using the GPU-enabled open-source Delft Advanced Research Terra Simulator (open-DARTS) under maximum and 2025-demand production schemes. Conditioning to GTD wells adds considerable data worth by constraining uncertainty in production well bottom-hole temperature (BHT) and pressure (BHP), while keeping injection pressure within Dutch regulatory limits. SIS models exhibit greater temperature and pressure variability than OBM models due to lower sand-body continuity. Despite large 80% confidence intervals, P50 production temperatures remain comparable for conditioned models. Distance-based generalized sensitivity analysis identifies net-to-gross ratio and the porosity–permeability correlation as dominant controls on thermal response. The 2025-demand scheme delays cold-front propagation. Results demonstrate that ensemble-based, GPU-accelerated high-spatial-resolution simulations enable robust and efficient uncertainty quantification for direct-use geothermal systems, highlighting the importance of well conditioning and reservoir heterogeneity characterization in constraining thermal responses.

1. Introduction

Geothermal energy has long been developed and utilized for electricity generation and heating applications, including greenhouse heating and direct-use heating (Lund and Toth, 2021). In the European Union (EU), more than 25% of space heating and cooling demand and more than 25% in greenhouses can come from geothermal energy (Ciucci, 2023). Geothermal energy in the Netherlands has considerable potential and is developing rapidly, and the Den Haag–Delft–Rotterdam area is a primary focus for geothermal initiatives due to the high energy demand from its dense population and greenhouses (Platform Geothermie et al., 2018).

The major geothermal plays in the West Netherlands Basin (WNB) include formations from the Triassic and Upper Jurassic/Lower Cretaceous periods (Mijnlieff, 2020). Initial efforts focused on the marine sandstones of the Vlieland Formation, followed by a rapid shift to the Delft Sandstone Member (DSSM) of the Nieuwerkerk Formation (Willems et al., 2020). The low-enthalpy direct-use geothermal project on the campus of the Delft University of Technology (under the consortium name "Geothermie Delft" - GTD) has been initiated to provide a unique research environment (Bruhn et al., 2015), alongside commercial thermal energy production for heating TU Delft's campus and parts of the city of Delft (Vardon et al., 2024). A geothermal doublet

* Corresponding author.
E-mail address: y.chen-21@tudelft.nl (Y. Chen).

https://doi.org/10.1016/j.geothermics.2026.103788
Received 23 February 2026; Received in revised form 5 June 2026; Accepted 17 July 2026
Available online 28 July 2026

Nomenclature

Acronyms

BHP	Bottom Hole Pressure
BHT	Bottom Hole Temperature
CI	Confidence interval
CNN	Convolutional neural network
DARTS	Delft Advanced Research Terra Simulator
DGSA	Distance-based Generalized Sensitivity Analysis
DSSM	Delft sandstone member
DUGS	Direct Use Geothermal Systems
ESP	Electric Submersible Pump
GPU	Graphics processing unit
GR	Gamma ray
GRFS	Gaussian random function simulation
GRU	Gate recurrent unit
GTD	Geothermie Delft
HPC	High performance computation
HSA	Hot sedimentary aquifers
KPCA	Kernel principal component analysis
LC	Lorenz coefficient
LSTM	Long short-term memory
N/G	Net-to-Gross ratio
NMR	Nuclear magnetic resonance
OBL	Operator-based linearization
OBM	Object-based modeling
PBM	Process-based Modeling
SGS	Sequential Gaussian Simulation
SIS	Sequential Indicator Simulation
TVD	True vertical depth
UQ	Uncertainty quantification
WNB	West Netherlands Basin

has been successfully drilled on TU Delft campus during the second half of 2023, and heat production started in February 2026. During the drilling campaign, well-log data, core data, and well-test data have been extensively collected (Barnhoorn et al., 2024). Despite these extensive data collection initiatives, the inherent complexity of geological uncertainty and limited spatial data away from the wells necessitate the use of computer models to gain a comprehensive reservoir-scale understanding.

In Direct-Use Geothermal Systems (DUGS), subsurface data is limited compared to oil and gas systems due to more marginal economics, making it more difficult to create a comprehensive geological model that fully captures subsurface complexity. Uncertainties stemming from input geological data, interpolation and extrapolation from data points, and a lack of knowledge on the existing geological structure (Wellmann et al., 2010) add extra difficulties to building a comprehensive geological model. 3D geological modeling consists of three stages: structural modeling integrating seismic and well log data, facies modeling using stochastic approaches and the petrophysical modeling constrained by facies models.

The distribution of rock physical properties, such as porosity and permeability, is guided by a geostatistical approach in areas away from the wells, while honoring the well data and being constrained by facies models. Different stochastic approaches, for example, Sequential Gaussian Simulation (SGS) (Journal and Alabert, 1989) or Gaussian random function simulation (GRFS) (Matheron, 1973), are utilized to model the distribution of rock physical properties under the facies constraints.

Reservoir heterogeneity is considered as the degree of variation of reservoir properties, e.g., permeability and porosity anisotropy at different scales (Tiab and Donaldson, 2016). Lorenz coefficient is a scalar used to describe the level of macroscopic heterogeneity in reservoirs (Tiab and Donaldson, 2016). Reservoir heterogeneity in hydraulic properties such as porosity has a large impact on the geothermal reservoir performance (Liu et al., 2019). The heterogeneity of the geological system can significantly affect the thermal response of a geothermal project (Major et al., 2023). A comprehensive uncertainty quantification (UQ) study (Wang et al., 2023) on a heterogeneous fluvial DUGS indicated that the simplification of the heterogeneity overestimates the production temperature. Besides, Aghaei et al. (2024) found that the fine scaled features such as basal lags and mud drapes within the fluvial meandering-belt sedimentary systems have minimal impact on the thermal production, if the proportion of the detailed features is small.

Numerous studies demonstrate that the role of facies architecture and connectivity in controlling cold plume propagation and the injection fluid flow has been widely demonstrated in both geothermal and hydrocarbon reservoirs, where connected high-permeability pathways accelerate flow channeling and early thermal or fluid breakthrough in fluvial systems (Gershenzon et al., 2014; C.J.L. Willems et al., 2017; Liotta et al., 2021; Aghaei et al., 2024). In meandering fluvial reservoirs, this threshold is typically recognized between 20% and 30% N/G (Larue and Hovadik, 2006). Meanwhile, in hydrocarbon production, Willis and Tang (2010) found that the models with fluvial channel belts having coarser-grained abandoned fills and significant vertical aggradation exhibit higher oil recovery factors, underscoring the importance of accurately characterizing facies connectivity within channel-belt architectures to improve reservoir performance predictions. Crooijmans et al. (2016) showed that fluvial geological models characterized by random, uncorrelated facies distributions yield different system lifetimes compared to those generated using stochastic process-based facies architectures in low-enthalpy geothermal systems. A CO_2 storage field test in a hierarchical fluvial point-bar system shows small-, intermediate- and large-scale connected sandstone channels forming a multiscale network that governs CO_2 invasion, spreading and breakthrough between wells (Zhou et al., 2020).

Numerical simulation is utilized to investigate the impact of macroscopic heterogeneity on the thermal response in presence of various uncertain parameters during the development of DUGS, which is often time-consuming. Previous uncertainty analysis (Wang et al., 2023) using a numerical simulation approach primarily focused on various reservoir parameters such as porosity, permeability, fluid properties, and economic factors without sensitivity analysis. A common solution to accelerate the computational time while maintaining the accuracy of the results is to upscale the property in spatial (Chen et al., 2003) or physical space (Hadjisotiriou and Voskov, 2025). Nevertheless, the question on how to effectively upscale heat conduction and convection in a geothermal production simulation still remains open (Perkins, 2019).

Consequently, resolving regional-scale reservoir heterogeneity necessitates the use of a large model comprising millions of grid cells with fine spatial resolution. With the advancement in computational hardware development, the Graphics Processing Unit (GPU) architecture has become a popular computing architecture to reduce simulation time. More efforts are made to facilitate the evaluation of geothermal exploration by leveraging the deep learning knowledge (Chen et al., 2025; Ullah et al., 2024; Qin et al., 2024). However, the objective of this study is not to develop or apply surrogate models, but to investigate uncertainty using high-fidelity, GPU-accelerated full-physics simulations. In this study, we use open-source Delft Advanced Research Terra Simulator (open-DARTS) (Voskov et al., 2024b) with an implementation of GPU architecture (Khait and Voskov, 2017) to perform full-physics geothermal simulation and improve computational efficiency. The verification of open-DARTS has been applied for various geothermal simulation applications (Khait and Voskov, 2019; Major et al., 2023; Wang et al., 2023) because of its proven efficiency and accuracy in solving complicated multi-phase, multi-component, thermal and chemical fluid flow problems for the given complex geological models. Wang et al. (2020) performed a benchmark study by comparing the simulation results to the results from AD-GPRS (Automatic Differentiation General Purpose Research Simulator) with geothermal module (Voskov and Zhou, 2015; Wong et al., 2015) and TOUGH2 (Pruess et al., 1999). The GPU version of open-DARTS has been successfully applied to perform a comprehensive UQ in the geothermal simulation application (Wang et al., 2023), showing that open-DARTS is well poised to simulate ensembles of stochastic forward simulations in a computationally efficient way.

Several studies collectively support the use of ensemble-based generalized sensitivity analysis, such as DGSA, to identify key geological controls on DUGS performance from a reservoir engineering perspective. This sensitivity analysis requires multiple computationally efficient forward simulations based on geological models defined at an appropriate problem scale. Previous uncertainty quantification studies have shown that geological parameters such as permeability and heat capacity strongly control geothermal system behavior, as demonstrated by Watanabe et al. (2010) using Monte Carlo analysis in deep crystalline reservoirs. Vogt et al. (2010) generated an ensemble of conceptual models that stochastically varied permeability without facies conditioning and showed that post-processing constraints reduce the uncertainty in thermal response. Feyen and Caers (2006) suggested that it is crucial to accurately characterize facies geometries to quantify the predictions of groundwater flow and transport for various levels of hydrogeological uncertainty. Based on the sensitivity analysis, the system complexity of the geothermal production in a deep mine is reduced by assigning constant values to non-sensitive parameters to guide an effective decision making for thermal production (Zhang et al., 2025). Zhang et al. (2026) also applied DGSA to evaluate the feasibility of data-target pairs for predictions in geothermal production.

Many efforts were also made to accelerate forward simulations of fluid flow in porous media, such as creating surrogate models by the kriging method (Mo et al., 2019) without preserving physics or reduced basis method preserving physics (Prud'homme et al., 2002). Using only the production well log (DEL-GT-01), Voskov et al. (2024a) filtered a small subset of geological models whose porosity at the well matched the measured log and used them to assess the impact of geological heterogeneity on thermal production. Chen et al. (2025a) investigated the thermal response of the Delft campus geothermal system using models with and without well-log conditioning; however, the limited number of dynamic simulations prevented statistical convergence.

This study specifically creates an ensemble of geological models following a complete geological modeling workflow: from horizon picking to property modeling to investigate the impact of geological uncertainty on thermal production. These parameters include the sand body content, facies geometry controls (e.g., channel width and depth), and property modeling parameters (e.g., semi-variogram ranges), which critically influence reservoir characterization and porosity-permeability correlation. By addressing the impact of these underexplored geological uncertainties on the thermal response, this work aims to provide deeper insights into their impact on reservoir heterogeneity and the dynamic behavior of the depositional environment where DUGS are mostly developed.

Nevertheless, a detailed heterogeneous geological model requires a fine grid resolution, which in turn demands greater computational resources. Besides the inherent depositional uncertainties, a second ensemble of geological models, using the same structural framework but excluding the Delft campus geothermal well data, was constructed to examine the data worth of hard well constraints on thermal performance. The wide range of uncertain geological modeling parameters and their complex interactions make it hard to evaluate the global importance of the thermal production. In this study, we use Distance-based Generalized Sensitivity Analysis (DGSA) to rank the global importance of uncertain parameters. Consequently, the sensitivity analysis provides insight into prioritizing the relevance of data to guide decision-making for projects in similar settings. Validation of subsurface models with heterogeneity is inherently challenging due to limited monitoring data. As the Delft campus geothermal project progresses and monitoring infrastructure is established, model validation will become feasible; further details are provided in Bruhn et al. (2026).

We present a comprehensive framework for simulating the thermal production of Delft campus geothermal wells using geological models constrained by the new well data. The objective is to assess how fluvial heterogeneity, characterized by various ranges of ranked geological input parameters, affects thermal performance of the DUGS and to quantify the value of additional data from the well logs to condition the pressure and temperature response. The workflow begins with the construction of a suite of 3D heterogeneous models by integrating seismic interpretation, well logs, and core data. We then assess model heterogeneity through static analysis, followed by dynamic simulations with a rigorous convergence and sensitivity analysis study. This systematic analysis aims to UQ reduction analysis under progressive data conditioning for the Delft campus geothermal project.

2. Research methods and design

This study utilized interpreted geological horizons, fault geometry and the well logs respecting the Delft campus geothermal well to construct a 3D structural model. The wells and associated well log data used in this study are listed in Table A1.1. An ensemble-based study was conducted to construct property models. The regional-scale property models were then cropped to the problem scale of numerical simulation on the GTD wells. Subsequently, a static analysis was performed on all cropped models to quantify their heterogeneity level. Next, the ensemble of cropped models is employed to simulate thermal production under two different production schemes: (a) the maximum rate and minimum injection temperature; (b) the current-demand rate and variational injection temperature. The energy demand and corresponding discharge rate/injection temperature were based on pre-2026 knowledge. Scheme (a) represents the maximum well capacity, reflecting the final project stage with additional demand, whereas Scheme (b) represents the current demand, where not all end users are yet connected to the heating network. At the same time, we performed a comprehensive sensitivity analysis using Distance-based Generalized Sensitivity Analysis (DGSA). Fig. 1 summarizes the workflow we are following in this work. Based on the workflow, five scenarios are outlined in the following Table 1. To facilitate the analysis, there are only OBM models unconditioned to the GTD data with porosity-permeability correlation (1) introduced to understand the data worth of constraining the uncertainties.

2.1. Geological setting and reservoir characteristics

The target aquifer of the Delft campus geothermal wells is Delft Sandstone Member (DSSM), which is part of the Nieuwerkerk Formation and consists of a fluvial succession formed during and after a major Early Cretaceous rifting phase in the WNB (Donselaar et al., 2015). The WNB is a 60-km-wide transtensional basin in the southwest of the Netherlands and adjacent offshore, consisting of a series of NW–SE trending structural highs and depressions. The Nieuwerkerk Formation consists of the Alblasserdam Member, DSSM, and Rodenrijs Claystone Member from deepest to shallowest. The interplay of accommodation space and sediment supply results in the high degree of variation in reservoir quality within the Nieuwerkerk Formation (Donselaar et al., 2015). Donselaar et al. (2015) found that the Alblasserdam Member formed through rapid deposition during active rifting, producing mostly fine overbank deposits, while DSSM developed with a balanced sediment supply and channel migration during a period of a tectonic

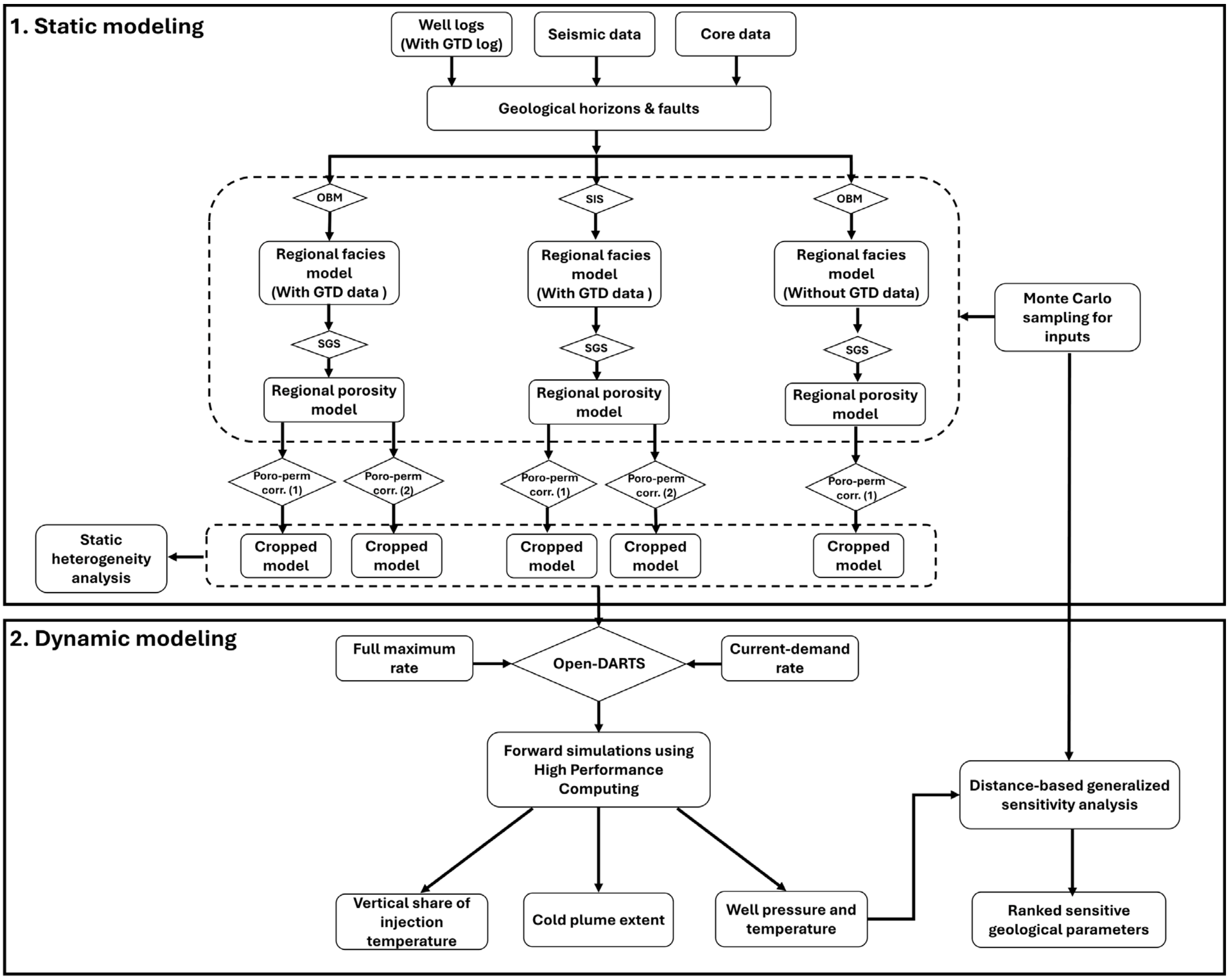

Fig. 1. The workflow covers the static geological modeling and dynamic simulations of the Delft campus geothermal project with a comprehensive sensitivity analysis on the geological parameters. GTD: Geothermie Delft; OBM: Object-based modeling; SIS: Sequential Indicator Simulation; SGS: Sequential Gaussian simulation; Poro-perm corr.: Porosity-permeability correlation where (1) and (2) indicate two different correlations.

Table 1
The scenarios integrating different modeling approaches (OBM, SIS) and different input data (GTD, poro-perm). For each combination of modeling approach and data, 400 equally probable models are generated for a total of 2000 models. GTD: Geothermie Delft; OBM: Object-based modeling; SIS: Sequential Indicator Simulation; SGS: Sequential Gaussian simulation; Poro-perm corr.: Porosity-permeability correlation where (1) and (2) indicate two different correlations.

Scenarios	Modeling approach	With GTD data	Poro-perm corr.	Nr. of models
1	OBM	Yes	(1)	400
2	OBM	Yes	(2)	400
3	SIS	Yes	(1)	400
4	SIS	Yes	(2)	400
5	OBM	No	(1)	400

quiescence. DSSM is considered to be a sand-rich reservoir having a large N/G ratio.

However, the sand distribution in the DSSM varies depending on the vertical and horizontal position within the reservoir due to the migration of channels from east to west over time (C.J. Willems et al., 2017). DSSM's reservoir quality varies spatially, but its average properties make it a good target aquifer. Prior to drilling the Delft campus geothermal wells, available well log data (TNO, 1977) indicated an average N/G of approximately 60% for the DSSM in the study area (Donselaar et al., 2015). However, logs from the DEL-GT-01 and DEL-GT-02-S2 wells drilled in 2025 as the producer and injector for the campus geothermal system, respectively, show N/G values exceeding 70% (Barnhoorn et al., 2024). The producer well reaches down to a depth of around 2290 m, resulting in an average initial reservoir temperature of 79 °C, aligned to the natural temperature gradient of 30 $\mathrm{K\,km^{-1}}$.

2.1.1. Structural model

Based on the regional geological setting, the top and bottom of the reservoir are interpreted from a merged and reprocessed seismic cube which was part of L3NAM1990C, L3NAM1985P and L3NAM1989K (Reinhard, 2019). The interpreted seismic/regional model was compiled by project geosciences. The data and interpretation will be made public in the future. The interpreted surfaces and a total number of 5 major faults, with geometrically consistent representation of subsurface structures (Caumon et al., 2009), were integrated to create a

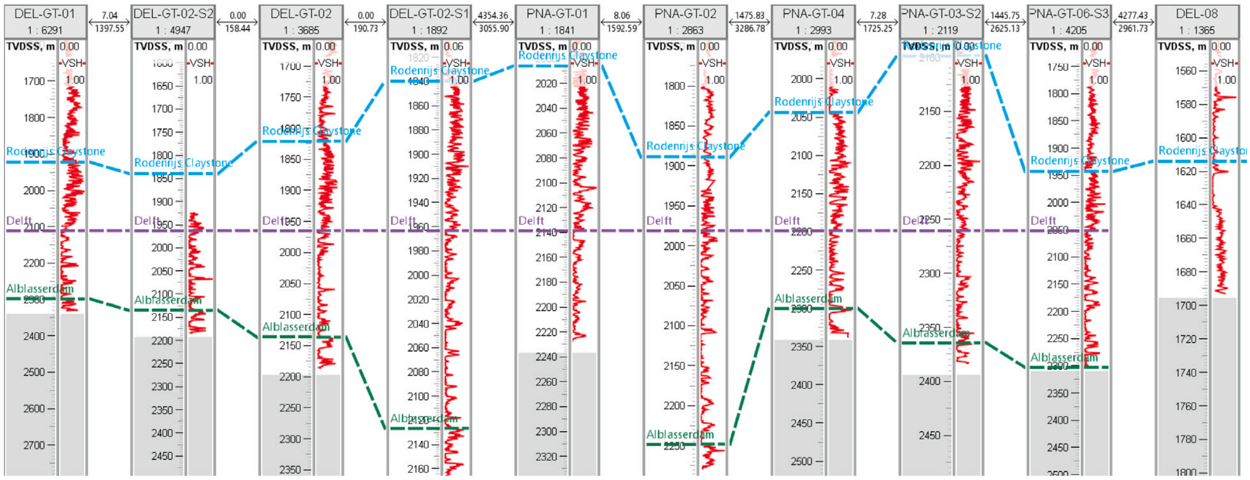

Fig. 2. The shale volume is calculated based on Gamma-ray (GR) logs from 10 wells, including the GTD doublet located in the WNB. The blue dashed line shows the Rodenrijs horizon, the purple dashed line shows the top of the Delft horizon and the green dashed line shows the top of the Alblasserdam horizon. (For interpretation of the references to color in this figure legend, the reader is referred to the web version of this article.)

3D structural geological model of the DSSM. The strike of interpreted faults shows a north-west to south-east trend which fits the primary orientation of the faults in WNB (Willems et al., 2020). The corner-point grid was chosen to better capture complex fault networks because of the flexible cell geometries. The 3D regional-scale structural model of the DSSM covers 47 km^2 and comprises ca. 23 million active grid cells, with a horizontal resolution of 20 m and a mean vertical resolution of 0.68 m, consistent with well-log resolution and recommended numerical setups for DUGS simulations (Chen et al., 2025b). A minimum zone thickness of 0.1 m and a minimum cell thickness of 0.25 m were enforced to stop zone bleeding and cell pinchouts adequately.

2.1.2. Facies model

This study used data from the Delft campus geothermal wells (Barnhoorn et al., 2024) to develop facies models. The thickness of the simulated reservoir layers at the well locations is 100 m – 150 m. We used gamma-ray (GR) logs to compute shale volume at the depth indicated in Fig. 2, because GR data is the only data present for all wells in the study area. We employed Stieber's model (Stieber, 1970) to estimate the shale volume based on GR data using the following two equations Eq. (1) and (2):

$$I_{\text{GR}} = \frac{\text{GR}_{\log} - \text{GR}_{\min}}{\text{GR}_{\max} - \text{GR}_{\min}}, \tag{1}$$

$$V_{\text{sh}} = \frac{I_{\text{GR}}}{3 - 2 \cdot I_{\text{GR}}} \tag{2}$$

where, I_{GR} [–] is the relative amplitude of the GR intensity, $\text{GR}_{\log}$ [API unit] is the gamma ray log values, $\text{GR}_{\min}$ [API unit] and $\text{GR}_{\max}$ [API unit] are the minimum and maximum gamma ray values respectively, V_{sh} [–] is the shale volume ratio. Fig. 2 shows the shale volume ratio of 10 wells within the study area.

We defined a discrete lithofacies log based on the shale volume ratio cut-off (Dejtrakulwong et al., 2009). Three ranges of shale volume ratio values identify three lithofacies: coarse sand, fine sand and shale to represent the major facies within the DSSM (Table 2). Coarse sand and find sand lithofacies are considered as reservoir-quality rocks. The 3D lithofacies distribution was fully conditioned to lithofacies logs. The lithofacies log derived from Fig. 2 is then blocked to the grid resolution using the most frequent facies occurrence in each block. We use these blocked lithofacies to constrain facies models. Then both Object-based modeling (OBM) and Sequential Indicator Simulation (SIS) are applied to simulate the lithofacies distribution. We derived semi-variogram parameters for the spatial continuity of facies within DSSM using 10 wells data listed in Table A1.1. Due to the limited data points in the

Table 2
Shale volume ratio based facies distribution.

Range	Lithofacies
$V_{\text{sh}} \leq 0.2$	Coarse sand
$0.2 < V_{\text{sh}} < 0.3$	Fine sand
$V_{\text{sh}} \geq 0.3$	Shale

minor direction, we used half of the range in major direction as the range in the minor direction to create horizontal anisotropic continuity of the properties to represent the nature of sedimentation (Caers, 2005).

Geological facies modeling is a fundamental approach in reservoir characterization, aiming to represent the spatial distribution of sedimentary facies in the subsurface (Ringrose, 2014). Object-based modeling (OBM) is a flexible approach to model the facies distribution through the use of geometric templates, for example channels, lobes, ellipses, or dunes, to create discrete objects in a model background (Holden et al., 1998). Objects of a predefined orientation and geometry are stochastically distributed into a neutral background within a given simulation grid. Target facies proportions are commonly derived from available well information, with geometric parameters being derived from well and analog data (Dreyer and Fält, 1993).

Sequential Indicator Simulation (SIS) is a pixel-based geostatistical method used to model categorical variables (Journel, 1983) such as facies by honoring spatial correlation patterns and well data (Goovaerts, 1997). It operates by sequentially simulating discrete categories (e.g., sand, shale) at unsampled locations using indicator kriging, ensuring that the resulting realizations reproduce the observed proportions and variogram structures of the facies (Deutsch and Journel, 1998). The common reservoir-quality facies of DSSM have been interpreted as point bar deposits (Donselaar et al., 2015) present in meandering systems, which are identifiable from the cores and well logs showing basal eroded surfaces and a fining upwards tendency, while the non-reservoir-quality facies are shale deposits on the floodplain in the fluvial systems (Wiggers, 2009).

2.1.3. Rock physics

In the study area, the porosity logs are only available from wells DEL-08 and PNA-13. These two conditioning wells are insufficient to construct a statistically robust experimental semivariogram for SGS. To avoid strong bias resulting from this limited porosity data, we used semi-variogram parameters derived from well facies data rather than porosity data, which are the primary input and control on the distribution of porosity using the SGS approach. Since there is no available permeability log for permeability modeling, we applied a porosity–permeability correlation, derived from core plug measurements focusing on DSSM and Nieuwerkerk formations (Willems et al., 2020). In this work, we used the porosity-permeability correlation of DSSM from Willems et al. (2020) as a reference. A second porosity-permeability correlation is derived from the Delft campus geothermal well log data (Barnhoorn et al., 2024), based on the nuclear magnetic resonance (NMR) well log data together with the definition of coarse sand, fine sand and shale in Table 2, to transform porosity into permeability. The NMR-derived permeability and porosity are divided into three clusters according to the threshold defined in Table 2. According to these three distributions, we separately derived two new porosity-permeability correlations for coarse sand and fine sand.

2.2. Lorenz coefficient

Once we obtained the property distribution, we evaluated the heterogeneity levels of all models using the Lorenz coefficient (LC). The Lorenz coefficient is calculated based on Lorenz curves, which is the relationship between normalized storage capacity Eq. (3b) and normalized flow capacity Eq. (3a). The values of LC range from 0 to 1, representing a completely homogeneous model at 0 and a fully heterogeneous model at 1.

$$C_k = \frac{\sum(kh)_i}{\sum(kh)_t} \tag{3a}$$

$$C_\phi = \frac{\sum(\phi h)_i}{\sum(\phi h)_t} \tag{3b}$$

Where i refers to the cumulative contribution of the first i grid cells after sorting all cells in descending order of flow capacity; t is the total contribution of all grid cells in the model domain.

2.3. Numerical model

DUGS are also called low-enthalpy systems, where water in the liquid phase is typically the main working fluid. The mass and energy conservation equations are taken to model the dynamic flow and transport processes during the field development and the open-source IAPWS-IF97 package is utilized to calculate the thermodynamic properties of water. General mass and energy conservation equations for a single-component two-phase geothermal system is expressed as follows:

$$\frac{\partial}{\partial t}(\phi \sum_{p=1}^{n_p} \rho_p) + \nabla \cdot \sum_{p=1}^{n_p} \rho_p s_p \vec{u}_p + \sum_{p=1}^{n_p} \rho_p \tilde{q}_p = 0, \tag{4}$$

$$\frac{\partial}{\partial t}(\phi \sum_{p=1}^{n_p} \rho_p s_p U_p + (1-\phi)U_r) + \nabla \cdot \sum_{p=1}^{n_p} h_p \rho_p \vec{u}_p + \nabla \cdot (\kappa \nabla T) + \sum_{p=1}^{n_p} h_p \rho_p \tilde{q}_p = 0 \tag{5}$$

where, t [day] is simulation time, s_p [–] is saturation of phase p, $\vec{u}_p$ [m s^{-1}] is velocity of phase p, ρ_p represents phase p phase density [kg m^{-3}], $\tilde{q}_p$ [m^3 d^{-1}]is the source term of the phase p, ϕ [–] is effective porosity, h_p is phase enthalpy [kJ kg^{-1}], κ is effective thermal conduction [kJ m^{-1} d^{-1} K^{-1}], U_p [kJ m^{-3}] and U_r [kJ m^{-3}] are phase p specific internal energy of fluid and rock internal energy respectively. The rock compressibility is computed based on the change of porosity:

$$\phi = \phi_0(1 + c_r(p - p_{\text{ref}})) \tag{6}$$

where ϕ_0 is the initial porosity [–], c_r is the rock compressibility [1/bar] and p_{ref} is the reference pressure [bars]. In addition, Darcy's law is applied to describe the fluid flow:

$$\vec{u}_p = -(\mathbf{K}\frac{k_{rp}}{\mu_p}(\nabla p_p - \gamma_p \nabla D)) \tag{7}$$

where $\mathbf{K}$ [mD] is the effective permeability tensor, k_{rp} [–] is phase p relative permeability, μ_p [mPa s] is phase viscosity, p_p [bars] is pressure of phase p, $\gamma_p = \rho_p g$ [N m^{-3}] is vertical pressure gradient and D [m] is depth. After neglecting the capillarity, we apply finite volume discretization and backward Euler approximation in time then we get following discretized form of Eqs. (4) and (5):

$$V[(\phi \sum_{p=1}^{n_p} \rho_p s_p)^{n+1} - (\phi \sum_{p=1}^{n_p} \rho_p s_p)^n] - \Delta t \sum_l (\sum_{p=1}^{n_p} \rho_p^l \Gamma_p^l \Delta\psi^l) + \Delta t \sum_{p=1}^{n_p} \rho_p q_p = 0, \tag{8}$$

$$V[(\phi \sum_{p=1}^{n_p} \rho_p s_p U_p + (1-\phi)U_r)^{n+1} - (\phi \sum_{p=1}^{n_p} \rho_p s_p U_p + (1-\phi)U_r)^n]$$
$$- \Delta t \sum_l (\sum_{p=1}^{n_p^l} h_p^l \rho_p^l \Gamma_p^l \Delta\psi^l + \Gamma_c^l \Delta T^l) + \Delta t \sum_{p=1}^{n_p} h_p \rho_p \tilde{q}_p = 0 \tag{9}$$

here V [m^3] is the control volume, Γ_p^l [mPa s m^2 d^{-1} bar^{-1}] is the convective transmissibility at the cell interface l, which is the combination of grid geometry and absolute permeability, ψ^l [bar] is the phase pressure, $q_p = \tilde{q}_p V$ [m^3 s^{-1}] is the fluid source/sink. Γ_c^l [mPa s m^2 kJ m^{-1} d^{-1} K^{-1}] is the heat conductive transmissibility at the cell interface l.

We resolve Eqs. (8) and (9) on the basis of an Operator-based Linearization (OBL) approach proposed by Voskov (2017) and used in the open-DARTS platform (Voskov et al., 2024b). Different operators are introduced: α is the accumulation operator, β is the flux operator, and θ is the source/sink operator. Those operators are the functions of vector $\mathbf{u}$ contains well-control variables, ω is the set of state variables, and ξ are the set of spatial coordinates.

$$\alpha(\omega) = \left(1 + c_r\left(p - p_{ref}\right)\right) \sum_{p=1}^{n_p} \rho_p s_p, \tag{10}$$

$$\beta(\omega) = \sum_p^{n_p} \frac{k_{rp}}{\mu_p} \rho_p, \tag{11}$$

$$\theta(\xi, \omega, \mathbf{u}) = \Delta t \sum_{p=1}^{np} \rho_p q_p(\xi, \omega, \mathbf{u}). \tag{12}$$

Then the discretized mass conservation Eq. (8) is written in the following operator-based residual form,

$$r(\xi, \omega, \mathbf{u}) = V(\xi)\phi_0(\xi)\left(\alpha(\omega) - \alpha\left(\omega_n\right)\right) - \sum_l \beta^l(\omega) \Delta t \Gamma^l \Phi_{p,ij} + \theta(\xi, \omega, \mathbf{u}) = 0 \tag{13}$$

here, the phase-potential-upwinding (PPU) strategy (Khait and Voskov, 2018a) is applied to model the effect of gravity:

$$\Phi_{p,ij} = p_j - p_i - \frac{\delta_p(\omega) + \delta_p(\omega_j)}{2}(D_j - D_i) \tag{14}$$

ω_j is the physical state of block j at the new timestep, $\delta_p(\omega)$ is the density operator for phase p.

Similarly, fluid energy accumulation operator α_{ef}, rock energy accumulation operator α_{er}, fluid energy advection operator β_{ef}, fluid thermal conduction operator γ_{ef}, and rock thermal conduction operator γ_{er} are formulated as functions of the state variable ω are formulated.

$$\alpha_{ef}(\omega) = (1 + c_r(p - p_{\text{ref}}))\left(\sum_{p=1}^{n_p} \rho_p s_p U_p\right), \tag{15}$$

$$\alpha_{er}(\omega) = (1 + c_r(p - p_{\text{ref}}))U_r, \tag{16}$$

$$\beta_{ef}(\omega) = \sum_p^{n_p} h_p^l \rho_p^l \frac{k_{rp}^l}{\mu_p}, \tag{17}$$

$$\gamma_{ef}(\omega) = (1 + c_r(p - p_{\text{ref}})) \sum_{p=1}^{n_p} s_p \kappa_p, \tag{18}$$

$$\gamma_{er}(\omega) = \alpha_{er}(\omega) \tag{19}$$

Table 3
Uncertain geological modeling parameters and distributions.
Note: The notation U[a, b] means the parameter has a uniform distribution, while [a, b] denotes discrete values.

Parameter name	Abbreviation	Distribution
N/G ratio	NTG	U[20%, 80%]
Maximum channel width	CW_MAX	U[192 m, 600 m]
Minimum channel width	CW_MIN	U[12 m, 30 m]
Semivariogram major range (Coarse sand/Sand)	CSNAD_MAJOR/SAND_MAJOR	U[362 m, 1086 m]
Semivariogram normal range (Coarse sand/Sand)	CSNAD_NORM/SAND_NORM	U[181 m, 724 m]
Semivariogram vertical range (Coarse sand/Sand)	CSNAD_VERT/SAND_VERT	U[5.89 m, 17.67 m]
Semivariogram major range (Fine sand)	FSAND_MAJOR	U[850 m, 1086 m]
Semivariogram normal range (Fine sand)	FSAND_NORM	U[212 m, 850 m]
Semivariogram vertical range (Fine sand)	FSAND_VERT	U[7.28 m, 21.84 m]
Maximum levee width fraction	LV_WIDTH_FRA_MAX	U[1.5, 2]
Minimum levee width fraction	LV_WIDTH_FRA_MIN	U[0.5, 1]
Maximum channel thickness	CH_THICK_MAX	U[4 m, 5 m]
Minimum channel thickness	CH_THICK_MIN	U[0.5 m, 1 m]
Maximum levee thickness fraction	LV_THICK_FRA_MAX	U[0.8, 1]
Minimum levee thickness fraction	LV_THICK_FRA_MIN	U[0.2, 0.5]
Maximum channel wavelength	WAVE_MAX	U[1000 m, 1200 m]
Minimum channel wavelength	WAVE_MIN	U[2000 m, 2400 m]
Maximum channel amplitude	AMPL_MAX	U[200 m, 300 m]
Minimum channel amplitude	AMPL_MIN	U[800 m, 900 m]
Maximum channel azimuth	AZIMU_MAX	U[260, 270]
Minimum channel azimuth	AZIMU_MIN	U[310, 330]
Porosity permeability correlation	POROPERM	[1, 2]

The operator-based residual form of the energy conservation equation is written as follows,

$$\begin{aligned} r_e(\xi,\omega,\mathbf{u}) &= \phi_0 V\left[\alpha_{ef}(\omega)-\alpha_{ef}(\omega_n)\right]+(1-\phi_0)VU_r\left[\alpha_{er}(\omega)-\alpha_{er}(\omega_n)\right] \\ &+\sum_l \Delta t\,\Gamma^l \Phi_{p,ij}\beta_{ef}(\omega) \\ &+\Delta t\sum_l \Gamma^l (T^i-T^j)\left[\phi_0\gamma_{ef}(\omega)+(1-\phi_0)\kappa_r\gamma_{er}(\omega)\right]=0 \end{aligned} \tag{20}$$

here T^i, and T^j are temperatures in blocks i and j and the operators in Eq. (20).

This operator formulation allows to represent complex physics in an algebraic system of equations with abstract operators. In this way, all expensive calculations can be done at the beginning with a few supporting points that can be reused across simulations. Later, the evaluation of the operators is based on a multilinear interpolation, which significant improves the performance at the linearization stage (Khait and Voskov, 2018b).

2.4. Model setup

Based on the geological settings and reservoir characteristics of DSSM, we utilized the geological parameters outlined in Table 3 to capture the variability in subsurface properties. These parameters are classified into three classes: (1) the proportion of sand, (2) channel properties and (3) porosity-permeability correlations. The channel properties range are summarized from Willems (2012), Gilding (2010). An ensemble-based approach is applied to create geological models to cover a wide range of global N/G ratio. The majority of simulation parameters are summarized in Table 4. Initial pressure and temperature follow natural gradients of 100 $\mathrm{bar\,km^{-1}}$ and 30 $\mathrm{K\,km^{-1}}$ respectively. Reservoir and non-reservoir rocks are distinguished using a porosity cutoff of 0.1, and four overburden and four underburden layers were added during simulation to ensure computationally efficient and realistic heat recharge (Chen et al., 2025b).

2.5. Dynamic response

2.5.1. System lifetime

Based on the production well Bottom Hole Temperature (BHT) from the numerical model, the system lifetime is defined as the time when the production well BHT drops by 5% of the difference between initial temperature (t = 0) and injection temperature, which is sensitive to capture the change in the production temperature:

$$\mathrm{T_{prod_{t=0}}} - \mathrm{T_{prod_t}} \le 5\% \times (\mathrm{T_{prod_{t=0}}} - \mathrm{T_{inj}}) \tag{21}$$

The definition of the lifetime as a 5% drop is meant to signal a sensitive, but observable change in production temperature and has been used in the past to standardize observations across different model types (Chen et al., 2025b; Daniilidis et al., 2020). However, a more accurate definition of the system lifetime should consider more parameters such as reservoir thickness and seismic hazard assessment.

2.5.2. Maximum injection well pressure

Dutch government (SodM and TNO, 2013) has a regulation defining the maximum injection well Bottom Hole Pressure (BHP) for a geothermal project as Eq. (22). This regulation considers an average pressure gradient with the depth multiplied by a constant as the upper boundary for injection pressure, without considering the in-situ stress under which the doublet operates.

$$\mathrm{BHP_{max}} = P_{\mathrm{reservoir}} + 0.0135 \times \mathrm{TVD_{reservoir}} \tag{22}$$

2.5.3. Vertical share of injection temperature

To understand the spatial spread of the cold plume, the vertical share of the injection temperature for all realizations was computed as follows Eq. (23).

$$V_s = \frac{\mathrm{T}_{init.} - \mathrm{T}_i}{\mathrm{T}_{init.} - \mathrm{T}_{inj.}} \tag{23}$$

where, $\mathrm{T}_{init.}$ [K] is the initial reservoir temperature of each reservoir grid block, T_i [K] is the reservoir temperature of each reservoir grid block at year i and $\mathrm{T}_{inj.}$ [K] is either constant injection temperature or varied injection temperature according to different production schemes. Two OBM realizations corresponding to the production temperatures of P10 and P90 at the maximum discharge rate (Table 4) were selected to represent the best and worst geological scenarios. Subsequently, a realistic demand-driven geothermal production scheme (Fig. A2.1), analogous to that applied in a geothermal project in Den Haag (Mottaghy et al., 2011) targeting DSSM, was implemented. The resulting vertical distribution of injection temperature was compared between maximum and variable discharge rate scenarios.

Table 4
Parameter settings for the reservoir model.

Parameters	Value
Regional-scale grid dimension, –	$341 \times 350 \times 200$
Cropped grid dimension	$172 \times 115 \times 200$
Grid size, m	$20 \times 20 \times (0.25 - 2.71)$
Permeability, mD	(0.004–2705)
Porosity, –	(0.05–0.35)
Reservoir-quality rock heat capacity, $\mathrm{kJ\,m^{-3}\,K^{-1}}$	2450 (Wang et al., 2021)
Reservoir-quality rock heat conductivity, $\mathrm{kJ\,m^{-1}\,d^{-1}\,K^{-1}}$	259.2 (Wang et al., 2021)
Non-reservoir-quality rock heat capacity, $\mathrm{kJ\,m^{-3}\,K^{-1}}$	2300 (Wang et al., 2021)
Non-reservoir-quality rock heat conductivity, $\mathrm{kJ\,m^{-1}\,d^{-1}\,K^{-1}}$	190.08 (Wang et al., 2021)
Temperature gradient, $\mathrm{K\,km^{-1}}$	30 (Békési et al., 2020)
Pressure gradient, $\mathrm{bar\,km^{-1}}$	100 (Verweij et al., 2014)
Injection temperature, K	298.15
Maximum discharge rate, $\mathrm{m^3\,d^{-1}}$	8400

2.6. Sensitivity analysis

Distance-based Generalized Sensitivity Analysis (DGSA) is based on clustering model responses from multi-dimensional inputs into several groups. The grouping is accomplished by using kernel techniques such as kernel principal component analysis (KPCA) or kernel clustering (Scheidt and Caers, 2009). Different clusters c_k are created. The L1-norm distance is then computed between the input CDF of each parameter X_i $(F(X_i))$ and the CDF of each parameter in each cluster $c_k(k = 1, 2, 3 \dots C)$ $(F(X_i|c_k))$:

$$\hat{d}_i^k = d_{L_1}(F(X_i), F(X_i|c_k)), \quad k = 1, 2, 3 \dots C; i = 1, \dots, n \tag{24}$$

Then, a bootstrap resampling technique is conducted to check if a parameter X_i has an effect on the response for a response cluster c_k. Resampling creates a distance distribution based on the given percentile α $(\hat{\hat{d}}_{i\alpha}^k)$. If the distance of parameter X_i in one cluster c_k $(\hat{d}_i^k)$ is larger than the resampling distance distribution $\hat{\hat{d}}_{i\alpha}^k$, it indicates parameter X_i is sensitive, which can be calculated by:

$$d_i^{\hat{s}(k)} = \frac{\hat{d}_i^k}{\hat{\hat{d}}_{i\alpha}^k} \tag{25}$$

The average sensitivity of one parameter X_i on the responses is computed as:

$$s(X_i) = \frac{1}{C} \sum_{1}^{C} d_i^{\hat{s}(k)} \tag{26}$$

The standardized sensitivity values are calculated utilizing pyDGSA, developed by Perzan (2025). If the standardized sensitivity value is high, the responses are sensitive to the input parameters. According to Park et al. (2016), parameters are considered critical if the bars overlap with the confidence interval (CI), and important if the bars lie partially within the CI. Production well BHT, injection well BHP, and production well BHP were considered to be three responses representing the performance indicators of DUGS to investigate the global effect of different geological parameters and porosity-permeability correlation on the thermal response of DUGS using the DGSA method for the given ensemble geological models which are constrained by the GTD well data, i.e. scenario 1–4 in Table 1.

3. Results and discussion

3.1. Geological model

3.1.1. Structural model

This study exclusively focuses on modeling DSSM, where two geological horizons: Top Delft and Top Alblasserdam (Fig. 3) are considered to create a 3D grid. Based on the existing seismic surveys, five major faults are involved in the structural framework. Both horizons and faults are utilized to ensure that the geological structure, stratigraphy, and discontinuities are faithfully represented in the simulation model.

3.1.2. Facies model

As shown in Fig. 4, the ranges in the major direction for shale, fine sand, and coarse sand are 385 m, 811 m, and 725 m, respectively. The corresponding vertical ranges are 4.5 m, 12 m, and 14 m.

We then extracted three facies proportion distribution from the models generated using OBM approach. This proportion information was utilized in SIS facies modeling to generate an ensemble of geological models, resulting in a similar range of reservoir-quality rock proportion as the OBM facies models. Fig. 5 shows the proportion of fine sand ranges from 11% to 32% while coarse sand ranges from 13% to 56%.

Row Fig. 6A shows the facies models created by different approaches with a similar reservoir-quality rock proportion of 50%. The channels are more continuous within the domain from the models created by OBM (Fig. 6A1) compared to the ones from the models created by SIS (Fig. 6A2), due to the fact that OBM method stochastically places the predefined channel geometry to the entire domain to satisfy the reservoir-quality rock proportion, while SIS is designed to look at a local neighborhood using pixel-based approach to match the predefined proportions. However, SIS is unable to model the high-order, long-range continuity property.

3.1.3. Property model

We then apply SGS to populate the porosity in different lithofacies using the semi-variogram information from Fig. 4 for both OBM and SIS models. Row Fig. 6B demonstrates the porosity models generated based on the facies models at row Fig. 6A. The porosity distribution shows that the channels in the OBM model are more continuous within the domain, while it is obvious that the channels in the SIS model are separated by shale lithofacies. This compartment potentially redirects the fluid and affects thermal production. Once we develop the full geological porosity model, it is cropped to a smaller region around the doublet. This cropped model contains ca. 4.1 million active grid cells, including the overburden and underburden layers for further study. With the cropped porosity model, the porosity-permeability correlations outlined in Section 3.1.4 are applied to map porosity to permeability.

3.1.4. Porosity-permeability correlation

The porosity distribution of fine sand overlaps significantly with the distribution of other lithofacies Fig. 7A. Fig. 7B and 7C clearly show that the new porosity-permeability correlation gives a higher permeability for the same porosity compared to the correlation from Willems et al. (2020). The difference strongly increases the permeability of porosity values less than 15% for both coarse sand and fine sand lithofacies because of the general good porosity and permeability of the GTD wells. We applied a porosity cut-off at 20% to prevent the fitted line from unrealistically exceeding 5 Darcy and to keep the trend flat. Bradley et al. (2025) described the details about using the NMR log to estimate the porosity and permeability for the GTD wells.

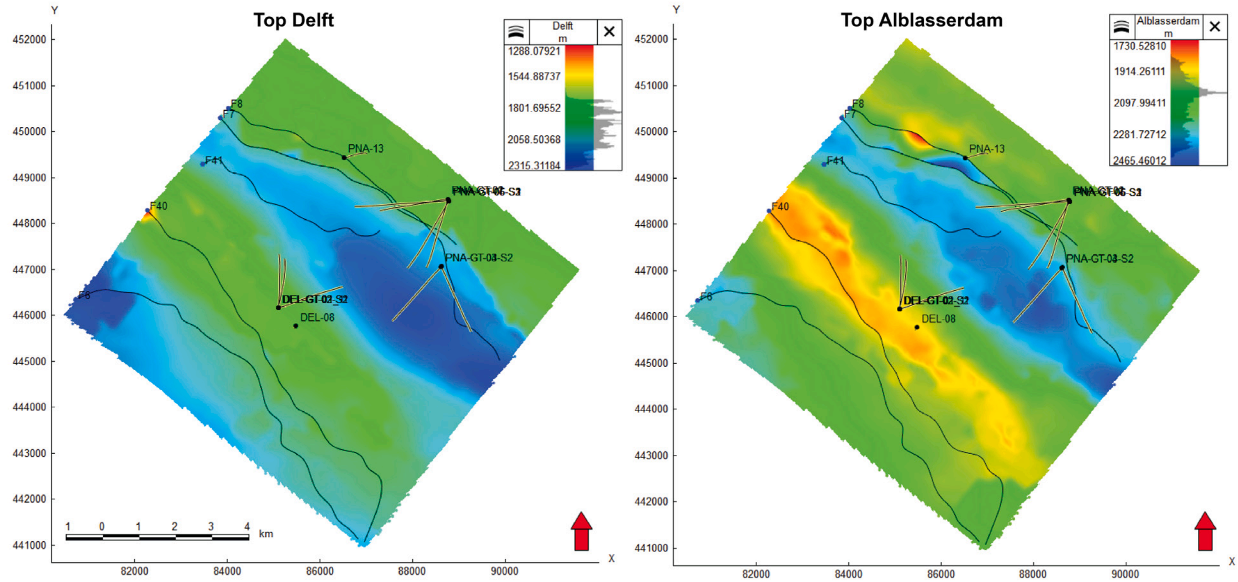

Fig. 3. The interpreted geological horizons and major faults in 2D. The color bar shows the depth of the surfaces. The black lines within the horizons indicate the location of five major faults within the study area, with the names of F6, F40, F41, F7 and F8 from left to right. (For interpretation of the references to color in this figure legend, the reader is referred to the web version of this article.)

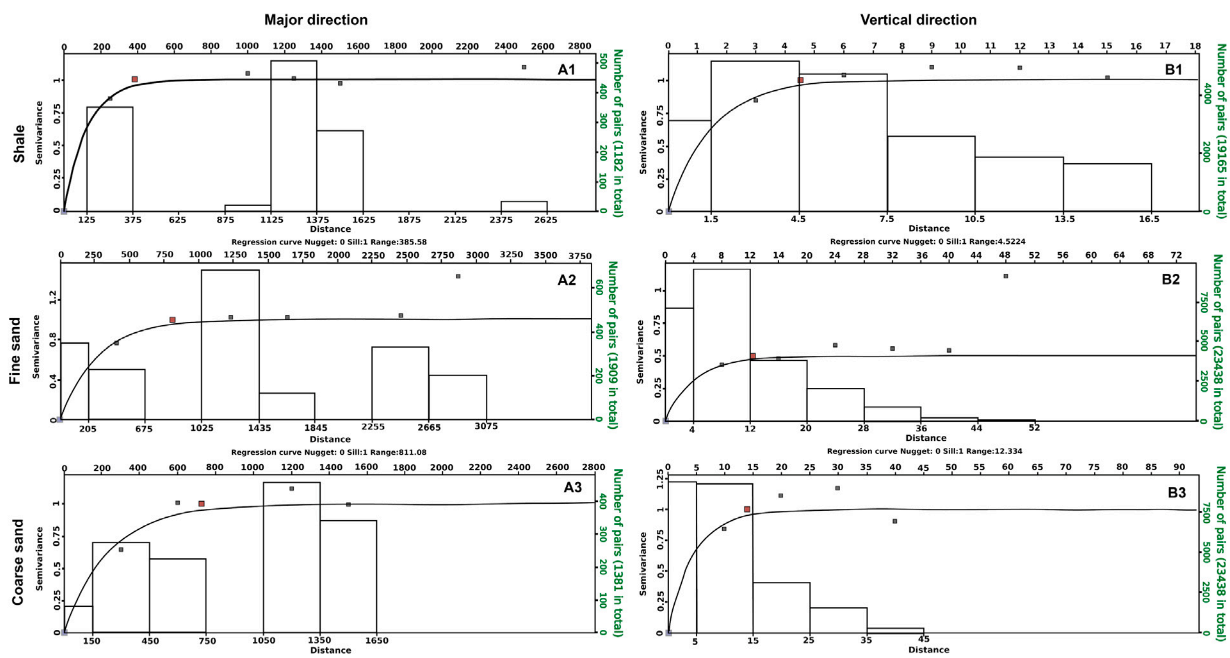

Fig. 4. The semivariograms depict spatial variability in shale (top), fine sand (middle), and coarse sand (bottom) for both the major (A1–A3) and vertical (B1–B3) directions.

3.1.5. Static heterogeneity analysis

We evaluated the heterogeneity of geological models across five scenarios listed in Table 1. Fig. 8 shows a large variation of LC, ranging from 0.28 to 0.74 across all scenarios. The broad distribution reflects that our geological models represent different degrees of heterogeneity, thereby capturing a significant amount of geological property uncertainty. When the models honor the GTD well data, Fig. 8 shows three-lithofacies SIS models have the widest range of LC values, while three-lithofacies OBM models have the narrowest range. The P50 of LC value is 0.53 in the three-lithofacies OBM models, which is similar to 0.55 from the three-lithofacies SIS models when the porosity-permeability correlation from Willems et al. (2020) is used. However, the overall distribution of LC values from the models created by the OBM and the SIS is different.

This difference comes from the underlying facies modeling approaches. OBM generates continuous channels that systematically enhance connectivity and preferential flow, resulting in consistently higher heterogeneity level across all realizations. In contrast, SIS populates facies cell by cell using a variogram-based geostatistical method, which produces fragmented and less connected channel bodies. As a result, three-facies SIS models can range from poorly connected systems with high LC to many realizations with higher connectivity with low LC, leading to a wider spread of LC. The comparison between the three-facies OBM models with and without GTD well data denotes that

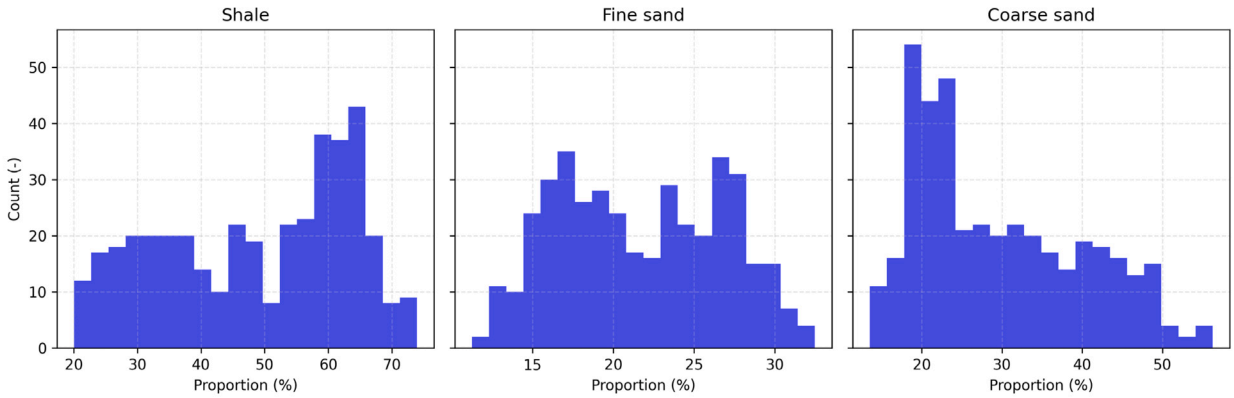

Fig. 5. The facies proportion distribution of models created using OBM approach.

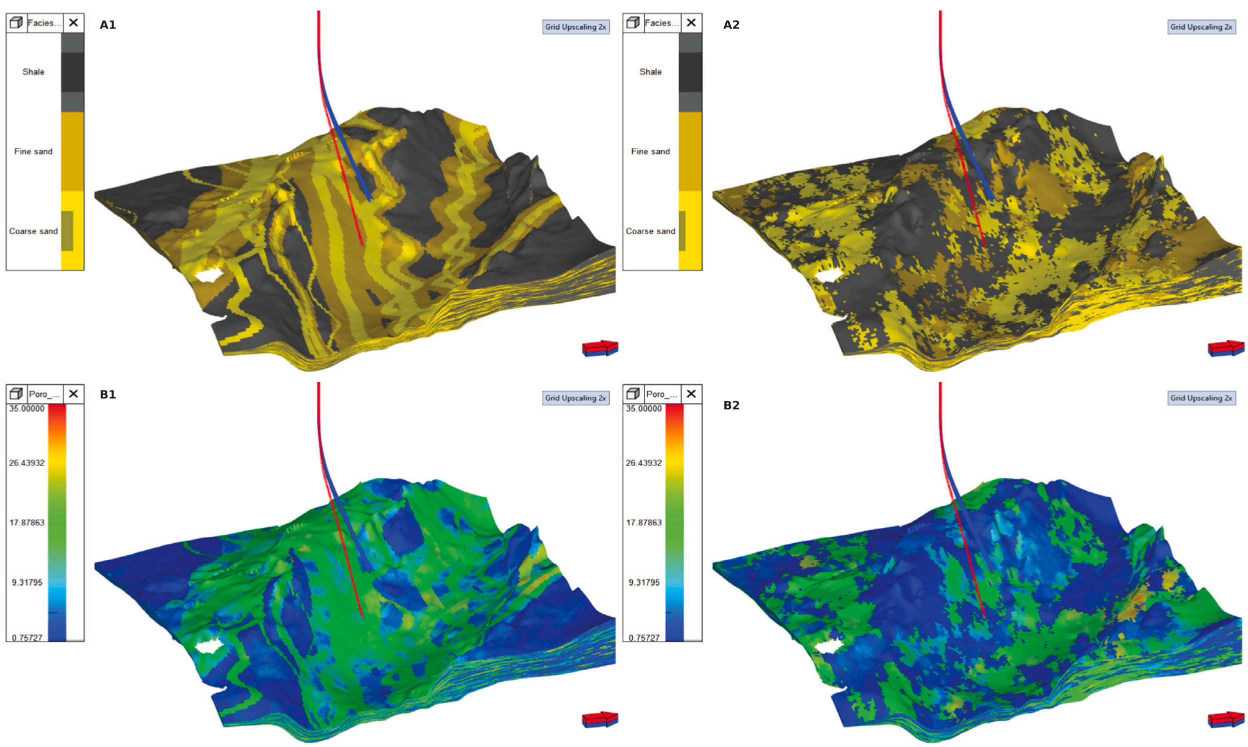

Fig. 6. Two regional-scale example models from the overall ensemble of 2000 models: Left-hand side using OBM showing facies (A1) and porosity (A2) and right-hand side using SIS showing facies (A2) and porosity (B2).

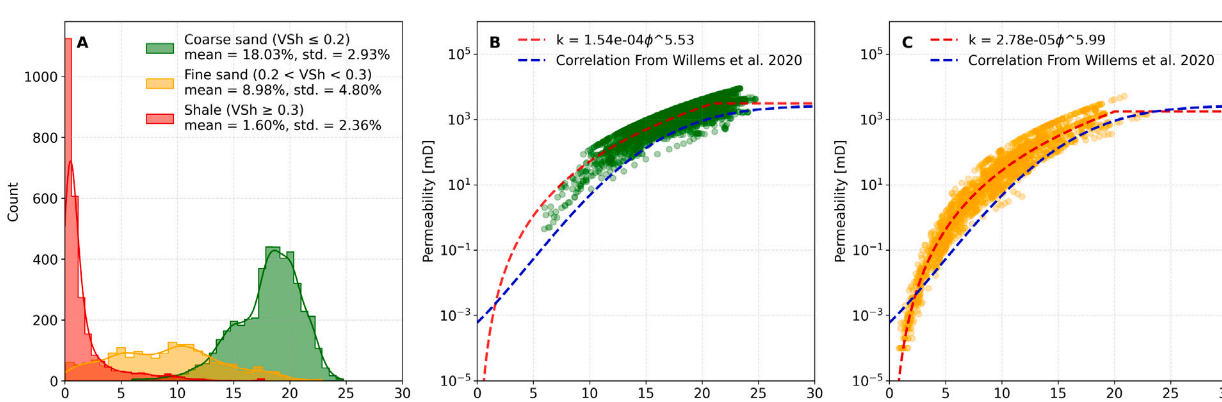

Fig. 7. A. NMR porosity distribution of the injector and the producer; B. NMR porosity and permeability data points and fitted lines for coarse sand lithofacies; C. NMR porosity and permeability data points and fitted lines for fine sand lithofacies.

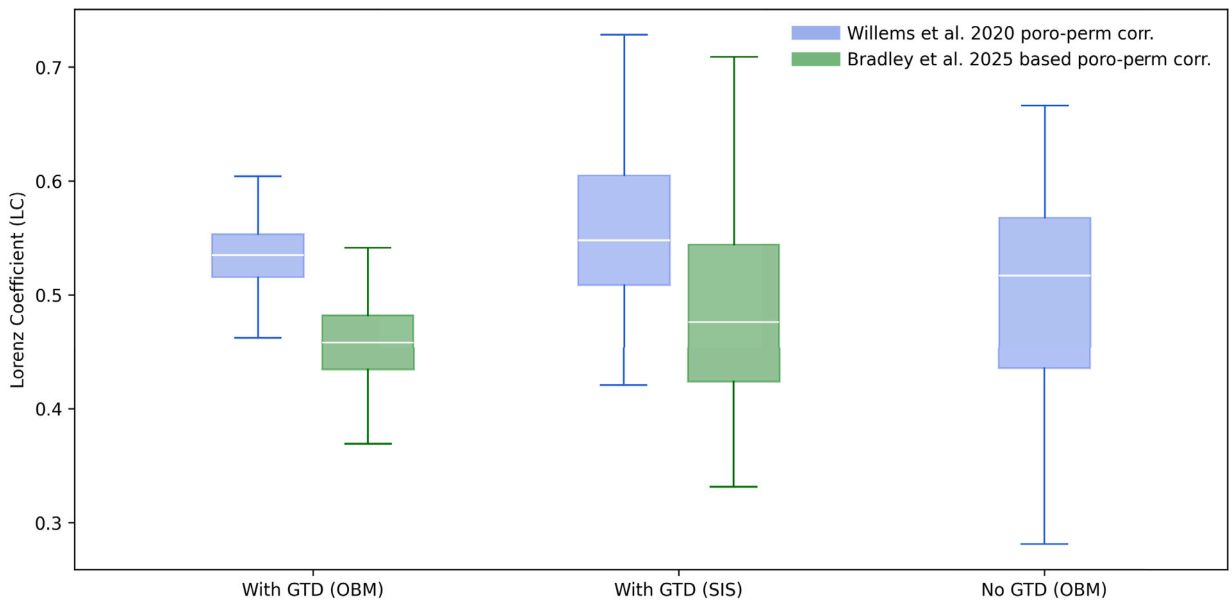

Fig. 8. Lorenz coefficient (LC) of all cropped geological models from all scenarios using different porosity-permeability correlation. Willems et al. (2020) poro-perm corr.: the correlation derived in Willems et al. (2020); Bradley et al. (2025) based poro-perm corr.: the correlation derived in this paper (Fig. 7).

the introduction of well data constrains facies distribution, resulting in more consistent channel geometries and a narrower distribution of LC. Meanwhile, removing GTD well data allows channels to be placed more randomly, leading to greater variability in connectivity between the injection well and the production well.

The introduction of the new porosity-permeability correlation moves all models towards lower LC values by comparing the blue and green distributions for the models created by OBM or SIS constrained by GTD well data. This decrease indicates that the models become more homogeneous through the use of the new porosity-permeability correlation, as the new correlation contrasts with the coarse sand and fine sand being less prominent compared to the correlation from Willems et al. (2020).

3.2. Dynamic analysis

3.2.1. Statistical convergence

In order to draw a solid statistical conclusion from the simulation results, a statistical convergence study is performed, which can be found in Fig. A3.1.

3.2.2. Well temperature and pressure

Regarding the effect of facies modeling approaches on the well output, different approaches have minimal impact on the P50 of BHT at the production well when all models are conditioned to the GTD well data, as indicated by the green dashed line (SIS models) and the blue dashed line (OBM models) in Fig. 9. However, the SIS models give a wider 80% CI of production well BHT and well BHPs. The wider BHP and BHT distribution indicates the connectivity between the injection well and production well differs more compared to that in the OBM models. The difference in connectivity between the SIS and OBM models comes from their fundamental modeling approaches: SIS models channels as discrete bodies based on geostatistical parameters, while OBM distributes channels continuously across the entire domain. Given the same amount of channel facies observed in the well data, the likelihood that the generated channel facies connect the injection and production wells differs between the two methods, due to the combined influence of semi-variogram parameters and reservoir-quality rocks. The connectivity variation in the SIS models is larger compared to the ones in the OBM models. Consequently, the SIS models show a wider BHP and BHT distribution. Models lacking Delft campus geothermal wells integration exhibit significant variations in BHT and BHP (Fig. 9A – C: red colors), despite employing the same modeling approach and the same number of lithofacies. Although the channel geometry of the cases with and without Delft campus geothermal well data is the same, their characterized heterogeneity differs, resulting in a slight difference in initial production temperature. The P50 of production well BHT from the models without GTD well constraints is lower compared to that including the GTD wells during the whole production period because the distribution of channels in the domain is different. It is most likely that fewer channels connect the injection and production wells in the models without constraints, allowing cold water to flow faster through them and bypassing a lot of the rock volume. For the scenarios with and without GTD well data constraints (scenario 2 and 5 in Table 1), all geological models share the same channel geometry (e.g., channel width, levee width, and channel azimuth) and the same N/G ratio range. The earlier thermal breakthrough and the increase in injection well BHP observed in scenario 5 indicate lower reservoir connectivity, given that all other geological settings remain unchanged. Scientific efforts are also directed to better seismic survey design and processing that would allow the imaging of channels in seismic data (Gesbert et al., 2025). Well testing can further help with constraining uncertainty by providing a higher level of confidence in estimates of aquifer transmissivity (Mijnlieff et al., 2013).

In contrast, the models constrained by Delft campus geothermal well data contain more channels, resulting in a more uniform and slower movement of cold water. We use the P50 production well BHT in Fig. 9 as the balanced case to estimate the system lifetime for each scenario using Eq. (21). The results show that the case without GTD well constraints has the shortest system lifetime of 23 years. Cases with constraints exhibit system lifetimes of circa 35 years.

The uncertainty in the number of connected channels in the models without GTD well constraints not only affects the production well BHT but also leads to a broader 80% CI for BHP. The maximum injection well BHP, determined in accordance with the regulation and under the assumption of an average reservoir depth of 2290 m, is ca. 260 bar. We evaluated the injection well BHP of all 780 models constrained by the Delft campus geothermal wells. The dynamic results show that about 91% of the geological models yield injection well BHP values below the regulation when using the full maximum rate. All models with injection

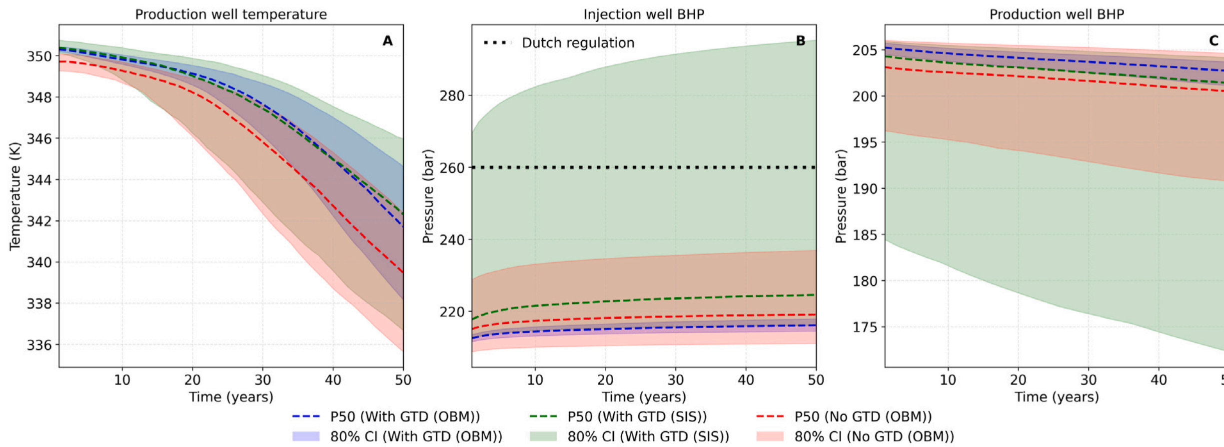

Fig. 9. Production data of the wells from different geological ensembles. The blue and green schemes represent the scenarios constrained by GTD wells' data with three lithofacies using OBM and three lithofacies using SIS, respectively. The red scheme shows the ensemble results of the scenarios without constraint of GTD wells' data with three lithofacies using OBM. The dashed lines indicate the P50 quartile of the data, while the shaded regions show the 80% confidence interval. (For interpretation of the references to color in this figure legend, the reader is referred to the web version of this article.)

well BHP values exceeding the limit coming from the three-lithofacies models created by SIS, which is attributable to the low connectivity between the injection and production wells.

Fig. 10 shows the temperature profile of the production well along the depth at different thermal production times for different geological scenarios. Each row starts with the temperature along depth according to the natural temperature gradient defined in Table 4. A distinct temperature change is observed at each well perforation in all cases after 5 years, which is a relatively short timescale for injected cold water to reach the production well located ca. 1500 m away. This temperature fluctuates because of the equilibrium between the cold water at the shallower and the warm water at the deeper reservoir layers respectively, due to the elevation of structural model after the thermal production starts. The jigsaw pattern means the temperature changes non-uniformly because of the vertical heterogeneity which is dictated by different porosity and permeability values at the perforation.

When the geological models are constrained by GTD well data, the temperature variations in three-lithofacies models created by SIS are more pronounced compared to the temperature variations in those created by OBM. This difference comes from the fact that the SIS utilizes different sizes of sand patches to represent the channels, resulting in a sand body discontinuity, while OBM models the channels continuously within the domain. The discontinuity of the sand away from the wells in SIS models redirects the cold water prominently, which leads to a more oscillating temperature. At year 40, the temperature profiles along depth for all realizations constrained by GTD wells data exhibit a maximum difference of 15 K, compared to a maximum difference of 23 K in the models not constrained by GTD wells data, by checking the A3 and C3 Fig. 10 respectively. The temperature variation range i.e. the difference between P10 and P90 at different time steps in Fig. 10 demonstrates first the models created by different facies modeling approaches result in different temperature variation ranges by checking row A and row B. Additionally, with the GTD well constraints added, the temperature variation range is smaller compared both row A and row C when the same facies modeling approach is used.

3.2.3. Sensitivity analysis

Fig. 11 indicates that N/G ratio and porosity-permeability correlation play dominant roles in controlling both BHT and BHP across scenarios conditioning to GTD wells, i.e., scenarios 1–4 in Table 1. Both production and injection well BHPs are primarily controlled by the porosity-permeability correlation, highlighting the importance of translating the porosity to permeability. The permeability has a large impact on the pressure. Meanwhile, the SIS models are more sensitive to facies proportions and porosity-permeability correlation. These results underscore the critical role of sand bodies connectivity and volume in governing pressure behavior near wells.

Fig. 12 shows that the proportion of reservoir-quality rock controlled by the N/G ratio in OBM models and by the coarse sand proportion in SIS models, together with the porosity–permeability correlation, has a critical impact on the production well BHT. This is because DUGS operate under forced convection, where thermal production depends mainly on the heat transported by flowing water. Most of this flow occurs within high-permeability lithofacies, which are governed by the high reservoir-quality rock proportions, although shales still contribute a little to heat transfer (Wang et al., 2021). The porosity–permeability correlation also plays a critical role in both scenarios. Facies distributions determine the geometry of sand bodies, within which porosity varies. Permeability is then derived from porosity through the chosen correlation, and it controls the ease of fluid flow. Introducing a different porosity–permeability correlation, therefore, alters the permeability field, which in turn modifies fluid flow and ultimately affects the production temperature.

Fig. 13 compares the relationship between geological heterogeneity and final production temperature for OBM and SIS models. For the OBM ensemble, Lorenz coefficients range approximately from 0.30 to 0.67, indicating a broad spectrum of heterogeneity. A negative linear correlation is observed between Lorenz coefficient and final production temperature: higher heterogeneity is associated with lower final production temperatures. This trend is particularly pronounced in realizations without GTD conditioning, which extend toward higher Lorenz coefficients and systematically lower temperatures. Differences between porosity–permeability correlations are visible but secondary compared to the effect of heterogeneity magnitude. For the SIS ensemble, Lorenz coefficients span a comparable range, but the temperature response exhibits a weaker monotonic trend. Production temperatures cluster within a narrower band for a given heterogeneity level, indicating a reduced sensitivity of thermal performance to Lorenz coefficient compared with OBM models. Conditioning to GTD data results in a modest upward shift in production temperature and a slight drop of the heterogeneity range. Overall, Fig. 13 demonstrates that geological heterogeneity exerts a strong control on long-term thermal performance in both OBM and SIS models. Lowering the heterogeneity slows down the cold plume propagation because of a larger sweeping volume for fluid flow. Conditioning to well data systematically reduces thermal responses uncertainty and shifts the ensemble toward higher production temperatures. These results highlight that both the

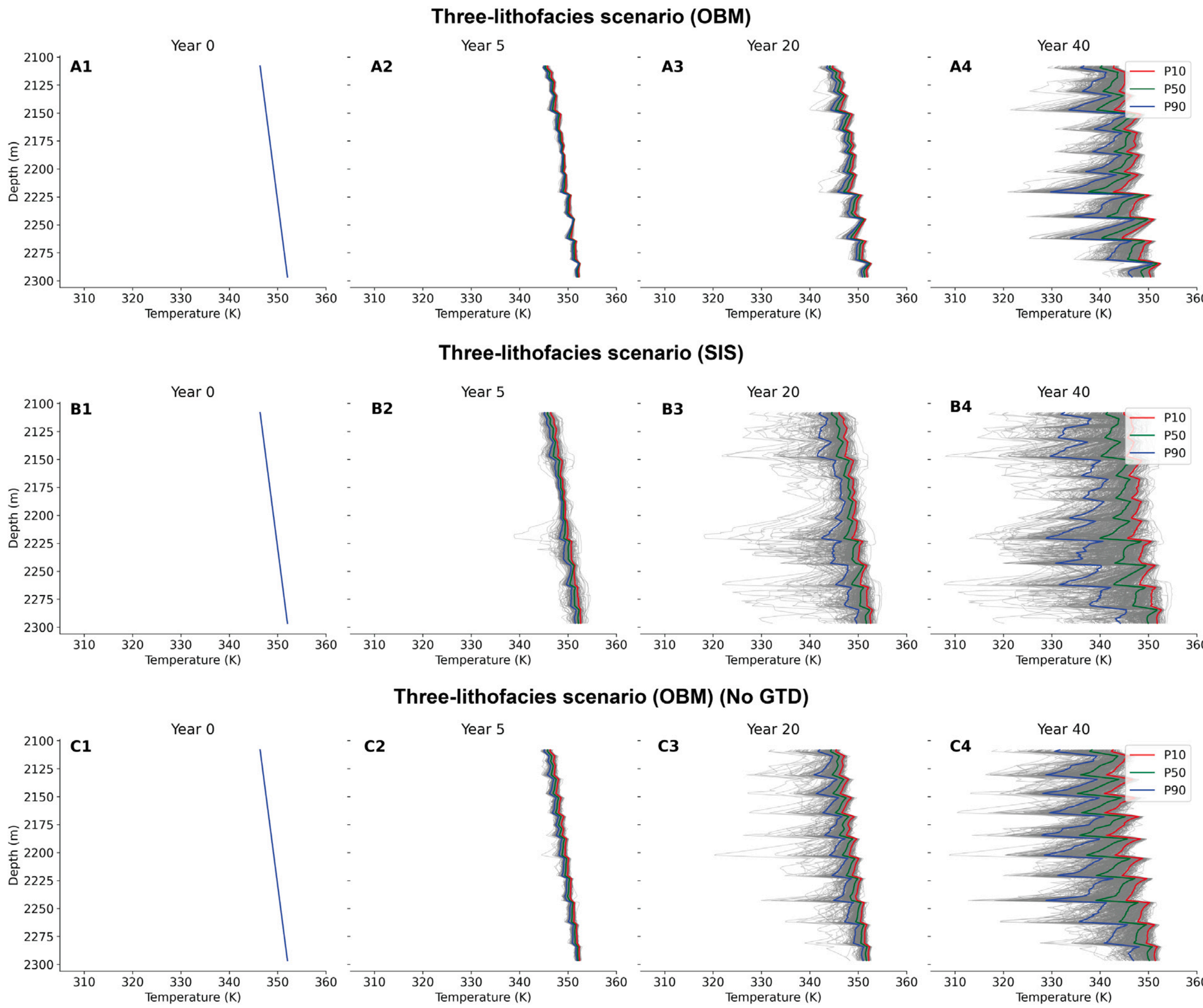

Fig. 10. The temperature distribution along the production well at year 0, 5, 20 and 40 for different scenarios.

modeling approach and the degree of data conditioning influence the propagation of geological heterogeneity into geothermal production forecasts.

3.2.4. Reservoir temperature and pressure

Fig. 14 shows the reservoir temperature and pressure changes, along with the permeability distribution, for the worst-case scenario among all geological realizations at the middle layer. We define the worst case as the geological realization that results in a production well BHT closest to P90 of production well BHT in Fig. 9. Fig. 14A1 shows that the injector and the producer are connected by highly permeable channels leading to a quick thermal breakthrough and a large temperature drop. The cold plume extent pattern in Fig. 14A2 appears regular because the N/G ratios at both the injection and production wells are high. As a result, most connected channels lie directly between the wells, creating a quasi-homogeneous flow pathway. This channel connectivity leads to a more uniform cold plume extent, consistent with the findings of Major et al. (2023), whose models with approximately 80% net-to-gross ratios exhibit similar behavior.

Rows A and B demonstrate that, despite using the same number of lithofacies, different facies modeling approaches yield distinct facies distributions. Consequently, they result in different porosity and permeability patterns, which are constrained by facies. In a three-lithofacies SIS model, the permeability (Fig. 14B1) has a scattered spatial distribution, with coarse sand facies (high-permeability regions) particularly dispersed. This contrasts with the more continuous distribution of coarse sand facies observed in an OBM model (Fig. 14A1).

The temperature distribution in Fig. 14B2 exhibits a more complex cold plume than in Fig. 14A2, primarily due to cold water freely flowing between the injection and production wells. Under the influence of forced convection, the cold water preferentially migrates through the scattered channel facies toward the production well, resulting in an irregular plume extent. Fig. 14B3 reveals a pronounced pressure difference compared to Fig. 14A3, characterized by a maximum pressure increase of 142 bar at the injection well and a maximum pressure drop of 33 bar at the production well. This outcome reflects the fact that SIS represents facies as patches of varying sizes according to the geostatistical models, creating a less continuous facies distribution around the wells and thus amplifying spatial pressure differences, even though the models in the first three columns are constrained by GTD well data.

The permeability distribution and dynamic outputs in row C differ significantly from those in row A when the geological model is unconditioned to the GTD well data, even though the same facies modeling approach and number of facies are used. Fig. 14C1 denotes that almost no highly permeable channels are placed in the direction of the injection well and the production well, although the reservoir-quality rock of the 3D geological models showing in Row C and Row A is similar as 50%. Fewer good connections between the injection and production wells in the models of row C result in a spiky cold plume (Fig. 14C2) and a large pressure difference (Fig. 14C3) compared to Fig.

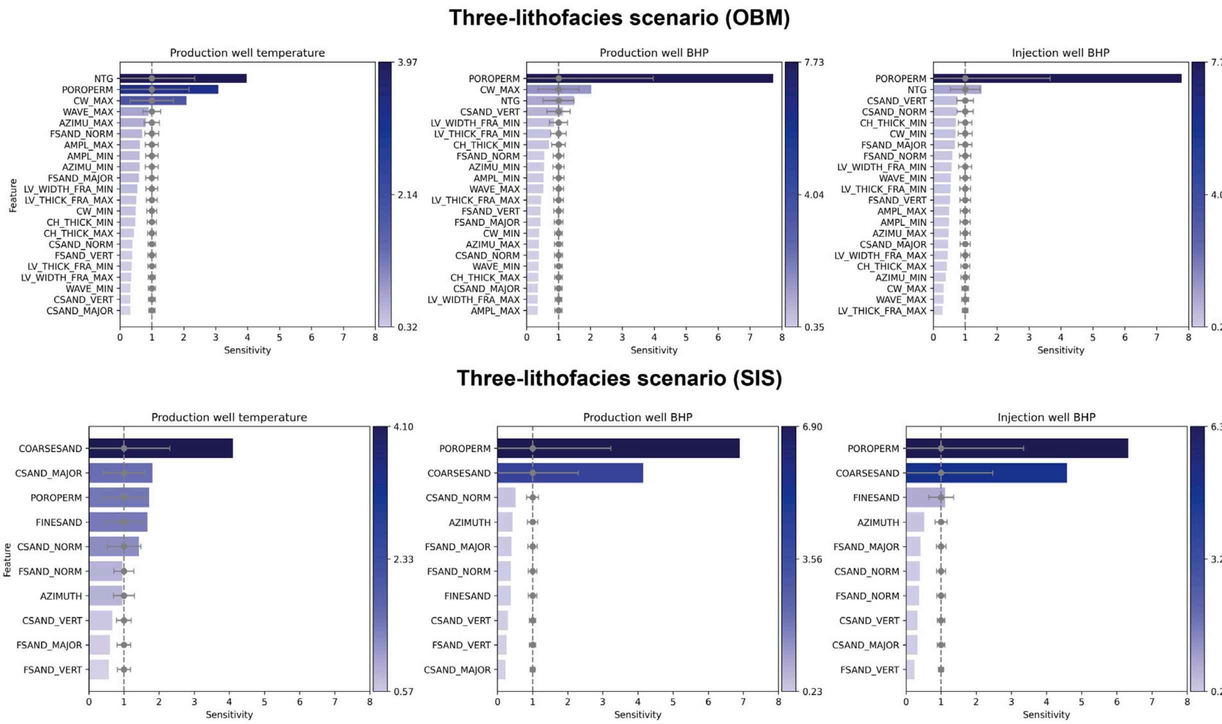

Fig. 11. Pareto plot of main effect with confidence interval (CI) for the models with three lithofacies created by OBM and SIS.

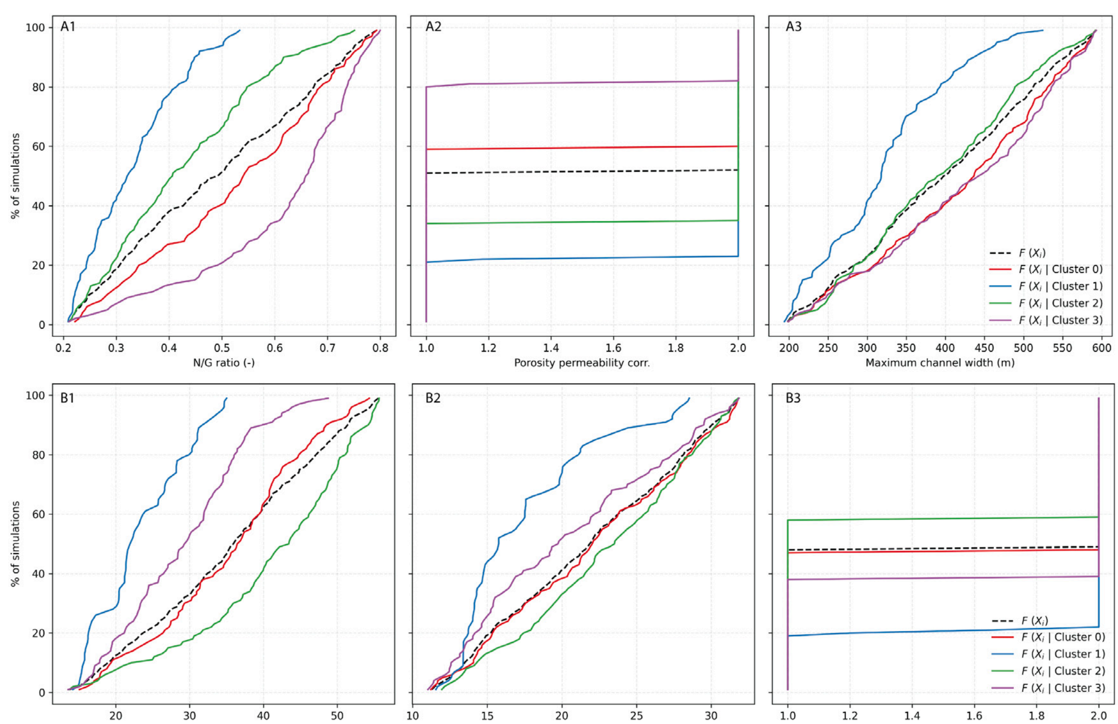

Fig. 12. Cumulative distribution functions (CDFs) of the top three most influential parameters on the production well BHT from the geological models with three lithofacies using OBM (A1 – A3), with three lithofacies using SIS (B1 – B3). Each subplot compares the distribution of the parameter within the three clusters (Cluster 0, Cluster 1, Cluster 2 and Cluster 3). The dashed line shows the prior CDF distribution.

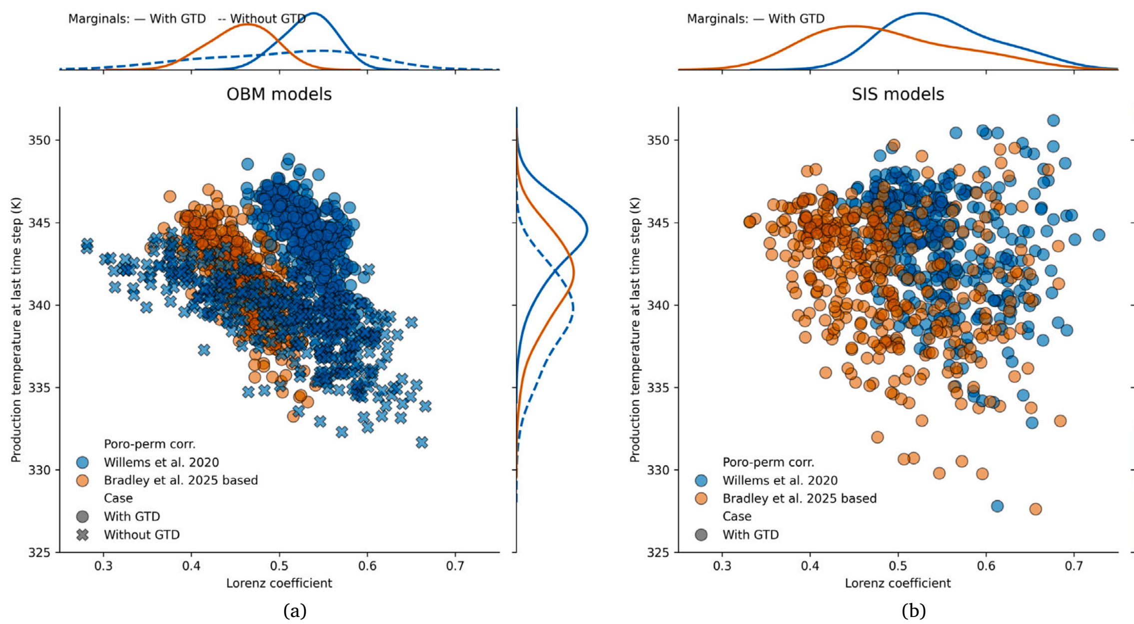

Fig. 13. Lorenz coefficient versus the production temperature at year 50.

14A2 and Fig. 14A3, respectively. In Fig. 14C2, the cold water flows in various directions before reaching high-permeability channels. In contrast, in Fig. 14A2, the cold water follows in channels that directly connect the injection and production wells, as more channels pass through both wells due to a high N/G ratio at both wells. The pressure change in Fig. 14C3 is much larger around the wells compared to Fig. 14A3, which has good connectivity between the injection well and the production well in models constrained by the GTD well data. Therefore, systematic connectivity analysis is essential in the development of low-enthalpy geothermal systems to enhance heat exchange, delay thermal breakthrough, sustain reservoir pressure, and minimize pumping losses (C.J.L. Willems et al., 2017). The comparison of reservoir temperature and pressure between row A and row C demonstrates that incorporating well data reduces uncertainty in dynamic simulation outputs, thereby enhancing the reliability of project development decisions. In future work, all results from the full-physics simulations, together with the sensitive parameters identified in Fig. 11, can be used as training data to develop surrogate models for more intensive optimization and uncertainty quantification in geothermal development.

3.2.5. Vertical share of the injection temperature

There are 20 SIS models out of 1200 geological models (scenario 2, scenario 4 and scenario 5 in Table 1) failed in simulations due to the extremely low connectivity between the wells. We assess the vertical share of the injection temperature of 1180 realizations with 200 reservoir layers using Eq. (23). Fig. 15 illustrates how injection temperature is vertically distributed in models created through different modeling approaches, both with and without GTD well data at three simulation time steps. Three-lithofacies OBM models with the constraints (the first row of Fig. 15) are the base for the following analysis. As shown in the second row of Fig. 15, the choice of facies modeling method significantly influences the vertical share shape, despite both the three-lithofacies OBM and SIS models being conditioned to the same well data. The differences in channel continuity significantly influence the sweep area, as DUGS forced convection-dominated systems.

In the models created by OBM, flow predominantly occurs within continuous channels that align with the direction between the injector and the producer, resulting in a more uniform vertical share pattern. In contrast, the discontinuity of sand bodies in SIS models causes the flow to disperse throughout the domain in search of favorable flow pathways, leading to highly irregular vertical share shapes across the entire model as time goes on. The distance between the injection well and the contour lines differs significantly between the two cases due to the more pervasive fluid distribution in the SIS models. In the SIS models, the likelihood of injection water reaching the production well is higher compared to the OBM models at the same time step. Even though the geostatistical parameters and the proportions of coarse and fine sand in the SIS models are directly derived from the three-lithofacies OBM models.

Row C of Fig. 15 shows that the OBM three-lithofacies models without conditioning to the GTD well data exhibit more dispersed and irregular vertical share shapes compared to the row A of Fig. 15. However, the overall trend remains similar, with the vertical share gradually narrowing and tapering toward the producer well, forming a more elongated and pointed shape. This elongation in both cases aligns with the general direction of the average channel azimuth. Incorporating the GTD wells helps to regularize the cold water flow within the domain. This is because the presence of GTD wells constrains the distribution of facies and porosity, which in turn influences the fluid flow patterns.

The average rate in the variational discharge rate case is 42% of the maximum discharge rate. This reduction slows the advancement of the cold front. After 30 years of thermal production, the distance between the injection well and the 90% contour line decreases by 41% to 48% when comparing Fig. 16A2–C2 and Fig. 16B2–D2. Such changes in the operational discharge rate introduce large uncertainty in the cold-front shape and eventually affect thermal production.

3.2.6. Time performance of geo-modeling and dynamic simulation with GPU

The regional-scale geological models (24 million grid cells) add extra computational overhead to the entire workflow (Fig. 1). Fig. 17 shows that, on average, it takes 11 min and 40 min using the OBM or the SIS approach respectively on a workstation with an Intel Core i9-10980XE CPU running Windows 10, to finish generating the full regional-scale facies and porosity models. OBM is more than 3

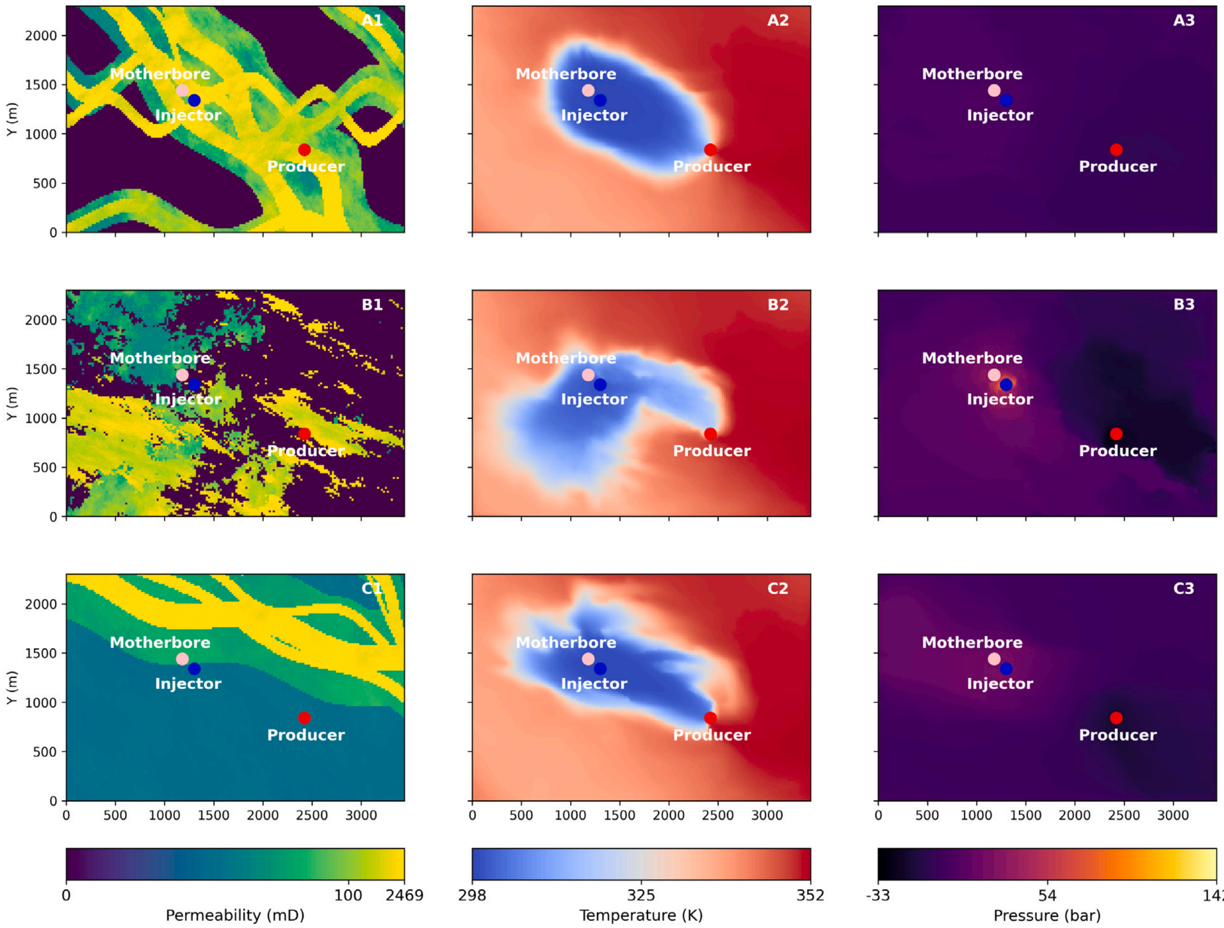

Fig. 14. The static and dynamic results of 3 out of 1200 realizations. Permeability distribution (the first column) and resulting temperature (the second column) and difference of the initial reservoir pressure and last time step reservoir pressure (the third column) distribution after 50 years' geothermal production at the middle of the reservoir. Row A shows the three-lithofacies OBM models under GTD wells' constraints. Row B presents the three-lithofacies SIS models constrained by GTD wells' data, and Row C illustrates the three-lithofacies OBM models without GTD well data constraints. The blue, pink, and red dots represent the injection well, abandoned well, and production well, respectively. The abandoned well, located at the north-west of the injection well, is also referred as the motherbore in Fig. 14. Note that due to the 3D heterogeneous nature of the modeled reservoir, the middle layer shown here is not able to convey the full complexity of the temperature and pressure evolution. (For interpretation of the references to color in this figure legend, the reader is referred to the web version of this article.)

times faster than SIS in generating geological models because SIS is a cell-by-cell approach requiring a significant number of covariance computations, while OBM stochastically places predefined geometric objects in the domain. Meanwhile, the dynamic simulation of this study involves solving approximately 8.2 million variables at a single timestep for a single geological model, with a total of 1955 models, making it computationally expensive. In this study, we utilize the Delft Blue Cluster (DHPC, 2024) and the flexible design of open-DARTS with an efficient parametrization using OBL and execution on GPU computing architectures. On average, simulating 50 years' thermal production using a single high-fidelity 3D heterogeneous model takes circa 3 min with the GPU version.

Simulation runtime is not directly comparable with previous work (Wang et al., 2023) due to differences in computational infrastructure: a dedicated GPU server was used previously, whereas this study employs a distributed HPC GPU system, resulting in longer runtime despite a shorter simulated period (50 versus 100 years). Although runtimes are 2.2 min and 3.2 min respectively, both remain within the same order of magnitude and are short in absolute terms. The GPU version of open-DARTS provides an order of magnitude speed-up compared to the geological modeling time. However, it is noticed that geological modeling operates on ca. 24 million grid cells, whereas simulation modeling involves ca. 4.1 million active grid cells. This work focuses on uncertain geological modeling parameters. There are more uncertain parameters, such as operational fluid properties, rock properties and economic inputs to be considered. The flexibility of open-DARTS opens a path to a comprehensive uncertainty quantification for the development of a real DUGS project (Daniilidis, 2024).

3.3. Modeling limitations

This study involves several geological and methodological assumptions that could pose some limitations. Reservoir properties are represented by upscaled porosity, implying that fine-scale depositional and diagenetic features e.g., draping and lamination are captured through averaged properties.

The framework further assumes that facies are the primary control on petrophysical variability, implying that heterogeneity is mainly expressed between facies rather than within facies. This common simplification may underestimate variability within the facies and small-scale heterogeneity. Aghaei et al. (2024) drew a similar conclusion that small-scale facies features have limited impact on DUGS production.

Additionally, the limited availability of porosity and permeability data from multiple wells constitutes one of key limitations of this study and should be addressed in future work to improve geological and petrophysical characterization.

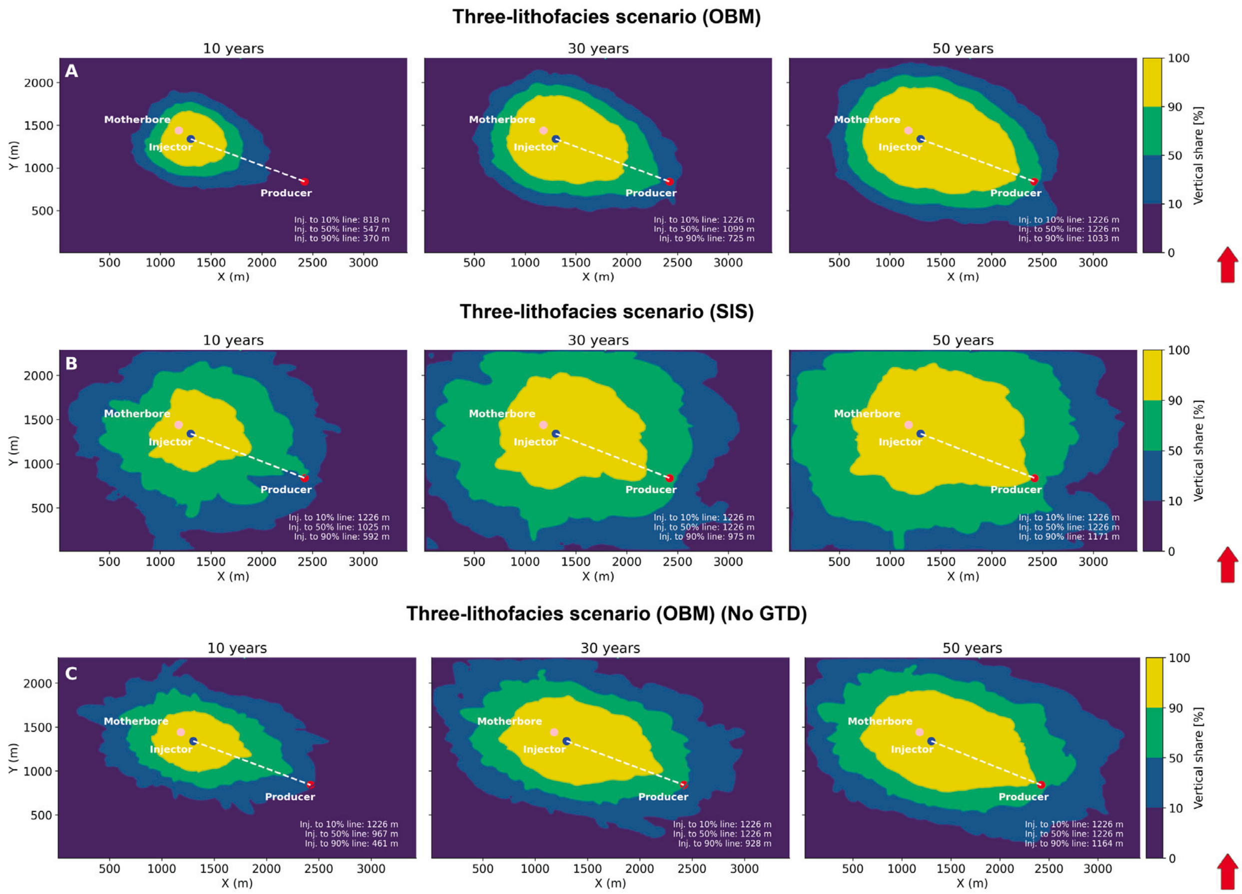

Fig. 15. Vertical share of injection temperature at xy plane for the cases constrained by GTD well data with three lithofacies using OBM (Row A), three lithofacies using SIS (Row B) and three lithofacies using OBM excluding the GTD well data (Row C) for different thermal production time (10, 30, 50 years). Red, blue and pink dots indicate the location of the production well, injection well and the abandoned borehole, respectively, at the middle reservoir layer. The values listed measure the distance from the injection well to different vertical share contour lines along the dashed white line that connects the injector and producer. The red arrow indicates North. (For interpretation of the references to color in this figure legend, the reader is referred to the web version of this article.)

Lastly, dynamic simulations based on the cropped geological models preserve the scale relevant to the problem. However, carrying out dynamic simulations using the full regional-scale geological models would be preferable, particularly in cases where multiple geothermal doublets operate within the study area, as this enables a more comprehensive assessment of doublet interactions.

4. Conclusions

In this study, a detailed ensemble of 3D heterogeneous geological models with an optimal numerical setup, both conditioned and unconditioned to the GTD data were generated. During the geological modeling stage, we utilized object-based modeling (OBM) and sequential indicator simulation (SIS) approaches to distribute the facies on the basin scale. Subsequently, we applied sequential Gaussian simulation (SGS) to populate the porosity in each lithofacies with extensive uncertain input of geological parameters. We then conducted a thorough static assessment of heterogeneity on the geological models using Lorenz coefficient (LC) to understand the impact of heterogeneity level on the thermal production using the newly introduced porosity-permeability correlation.

For the 1955 stochastic forward simulations, the mean runtime per simulation stabilized at ca. 3.2 min using the parallel GPU implementation of open-DARTS. After this, we utilized the moving average values of production well Bottom Hole Temperature (BHT) as an indicator to check the convergence of the simulation ensemble and draw an informative statistical conclusion. The cold plume extent, reservoir pressure and vertical share of the injection temperature are evaluated following the comprehensive sensitivity analysis using the well outputs.

Although this study based on the Delft campus geothermal project, the proposed workflow is applicable to a wide range of subsurface energy systems where geological uncertainty and data conditioning play a critical role. Five generalizable learnings emerge from the ensemble simulations.

1. **The choice of facies modeling method is itself a first-order uncertainty source.** Object-based modeling (OBM) and Sequential Indicator Simulation (SIS) produce systematically different spatial distributions of reservoir temperature and pressure, even when the models are conditioned to the same well data. This means that fixing a single modeling method and focusing effort on parameter sensitivity analysis within that method will underestimate total uncertainty. Future studies should treat the method to creating conceptual geological models as an explicit uncertainty dimension, particularly where sand body connectivity is poorly constrained.
2. **Well conditioning reduces pressure uncertainty far more than thermal uncertainty.** Conditioning geological models to well data substantially narrows uncertainty, but the effect is strongly asymmetric: pressure responses are much more tightly constrained than temperature responses. This has a practical implication for project risk assessment that even with good well coverage, thermal performance predictions will remain substantially more uncertain than pressure-based indicators such as

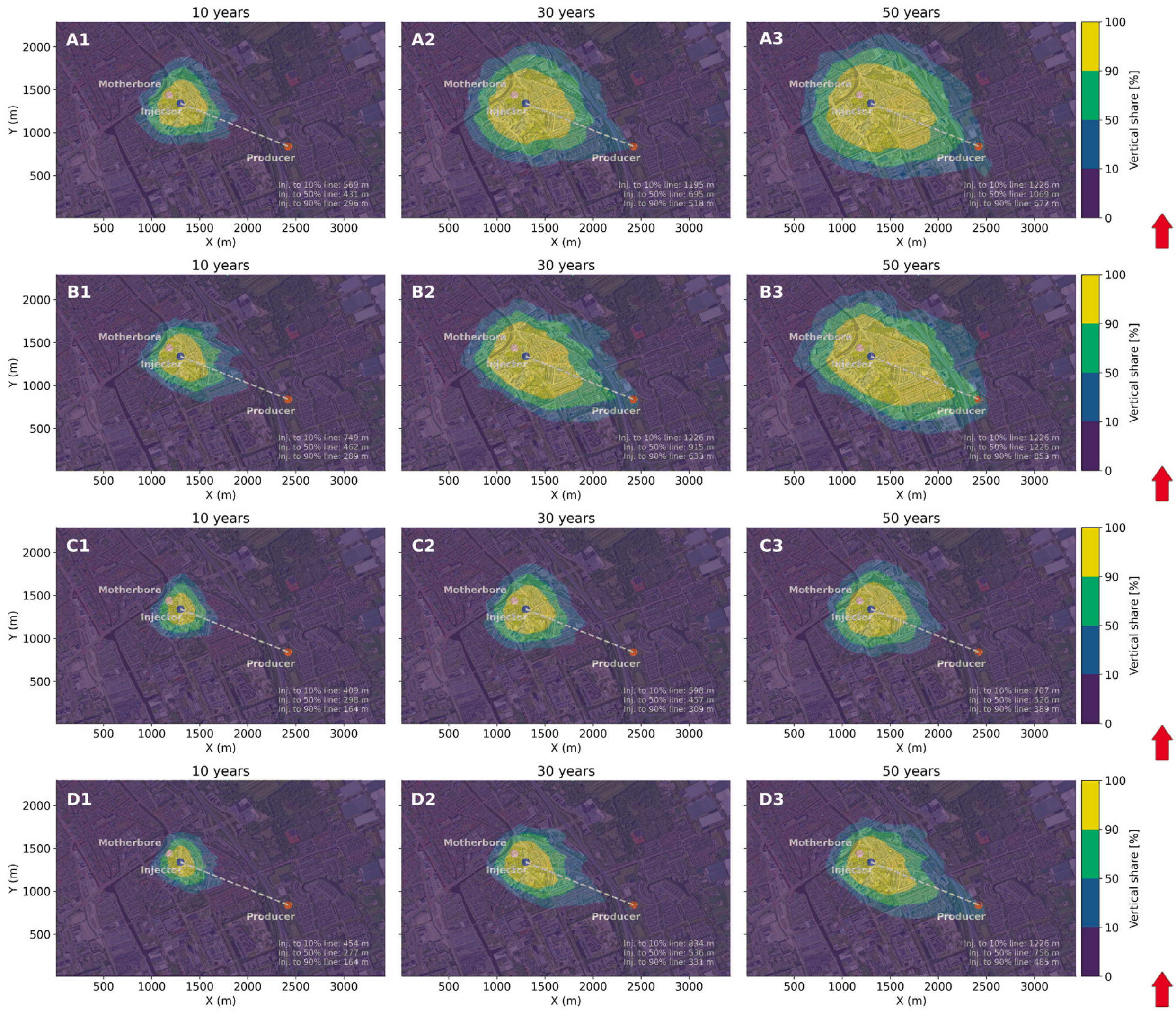

Fig. 16. Vertical share of injection temperature under different operational discharge rates, with a satellite map of part of Delft shown at the top. Row A shows the geological model with the latest thermal breakthrough at the maximum discharge rate; Row B shows the geological model with the earliest thermal breakthrough at the maximum discharge rate; Row C & D show the geological model with the latest and earliest thermal breakthrough under the current-demand discharge rate, respectively.

injection well bottom hole pressure (BHP). Studies should not assume that well conditioning provides equivalent uncertainty reduction across all production metrics.

3. **Reservoir heterogeneity level is a strong early predictor of thermal performance spread.** The Lorenz coefficient shows a strong negative linear correlation with final production temperature in OBM models. This offers a practical screening tool: heterogeneity can be quantified from static geological models before running any flow simulations, allowing rapid identification of geological realizations most likely to produce extreme thermal outcomes. Incorporating heterogeneity assessment as a standard pre-simulation quality check could improve the efficiency of ensemble workflows in any DUGS project.
4. **A small set of parameters dominates production response while most inputs are insignificant.** Distance-based generalized sensitivity analysis (DGSA) consistently identifies N/G ratio (in OBM) or sand proportion (in SIS), together with the porosity-permeability correlation, as the dominant controls on both thermal and pressure performance. The majority of other property modeling parameters have negligible influence. This supports a focused uncertainty quantification strategy: rather than sampling broadly across all geological parameters, future studies can prioritize rigorous characterization of these controlling inputs — particularly the choice and calibration of the porosity-permeability transform — while simplifying treatment of less influential parameters.
5. **Ensemble sizes of circa 400 realizations are sufficient for robust statistics analysis at this complexity level.** Convergence of the P10, P50, and P90 moving averages of production well bottom hole temperature (BHT) demonstrates that approximately 400 geological realizations per scenario are sufficient to draw statistically robust conclusions. This provides a practical benchmark for ensemble sizing in similar subsurface uncertainty studies, balancing computational cost against statistical reliability. The result also supports the use of GPU-accelerated simulators as a viable path to making large ensembles tractable for operational decision-making in a development of DUGS.

Together, these conclusions suggest that the path to more reliable geothermal performance predictions lies less in refining individual parameter distributions and more in rigorously addressing geological modeling choices: facies modeling methods, the heterogeneity level of the models, and porosity-permeability correlations that significantly affect all downstream outputs.

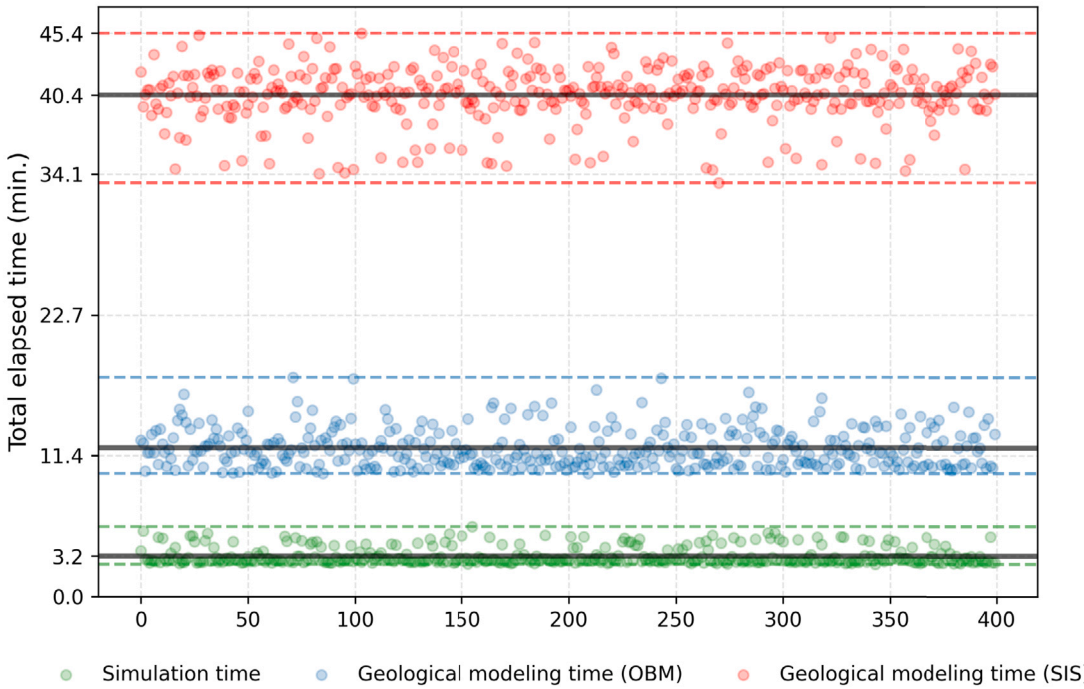

Fig. 17. The geological modeling time of 400 regional-scale models with ca. 24 million grid cells versus the simulation time of 400 cropped OBM models with ca. 4.1 active grid cells using the GPU version (green dots) of open-DARTS. The blue dots indicate the geological modeling time using OBM, and the red dots show the geological modeling time using SIS. The black solid line represents the mean simulation time for three cases. (For interpretation of the references to color in this figure legend, the reader is referred to the web version of this article.)

CRediT authorship contribution statement

Yuan Chen: Writing – review & editing, Writing – original draft, Visualization, Validation, Software, Methodology, Investigation, Formal analysis, Conceptualization. **Guillaume Rongier:** Writing – review & editing, Methodology, Investigation, Formal analysis, Conceptualization. **James Robert Mullins:** Writing – review & editing, Investigation. **Denis Voskov:** Writing – review & editing, Supervision, Methodology, Investigation, Conceptualization. **Alexandros Daniilidis:** Writing – review & editing, Supervision, Project administration, Methodology, Investigation, Funding acquisition, Formal analysis, Conceptualization.

Declaration of generative AI and AI-assisted technologies in the manuscript preparation process

During the preparation of this work the author(s) used ChatGPT in order to improve the sentences readability. After using this ChatGPT, the author(s) reviewed and edited the content as needed and take(s) full responsibility for the content of the publication.

Declaration of competing interest

The authors declare that they have no known competing financial interests or personal relationships that could have appeared to influence the work reported in this paper.

Acknowledgments

We would like to thank Rock Flow Dynamics for the provision of the academic license to tNavigator and Delft University of Technology for the financial support. Additionally, the authors sincerely thank the three anonymous reviewers for their constructive and critical comments, which significantly improved the quality of this manuscript. We are grateful to Susanne Laumann for coordinating access to and the use of the Delft Campus well data. We also thank Tom Bradley and Auke Barnhoorn for the insightful discussions on well log interpretation. Finally, we acknowledge the support of all members of the Geothermie Delft project, whose collaboration and contributions made this work possible.

Appendix

A.1. Well data used in creating geological models

See Table A1.1.

A.2. Geothermal energy production, discharge rate and return temperature

The realistic production data is from the operators' calculation based on the maximum power of Electric Submersible Pump (ESP),

Table A1.1
A list of the wells and availability of log data used to create regional-scale facies and porosity models. GR: gamma ray; NPHI: neutron porosity. The words in bold mean that the data is present and used in the modeling.

Borehole	Year	Well logs	
		GR	NPHI
DEL-GT-01	2023	**GR**	**NPHI**
DEL-GT-02	2023	**GR**	
DEL-GT-02-S1	2023	**GR**	
DEL-GT-02-S2	2023	**GR**	**NPHI**
PNA-GT-01	2010	**GR**	
PNA-GT-02	2010	**GR**	
PNA-GT-04	2010	**GR**	
PNA-GT-03-S2	2010	**GR**	
PNA-GT-06-S3	2018	**GR**	
DEL-08	1994	**GR**	**NPHI**
PNA-13	1977	**GR**	**NPHI**

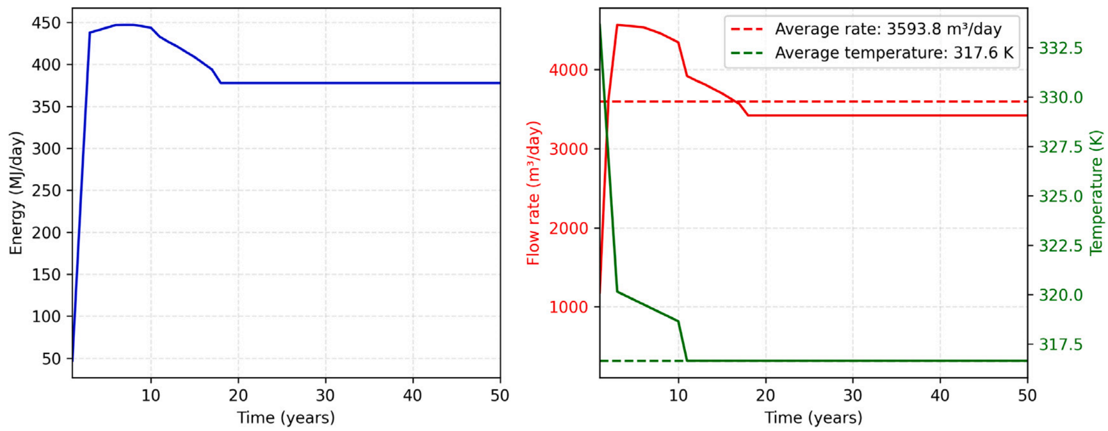

Fig. A2.1. Left: the energy out per year from the Delft campus geothermal project; Right: the return temperature of the injection water and derived discharge rate.

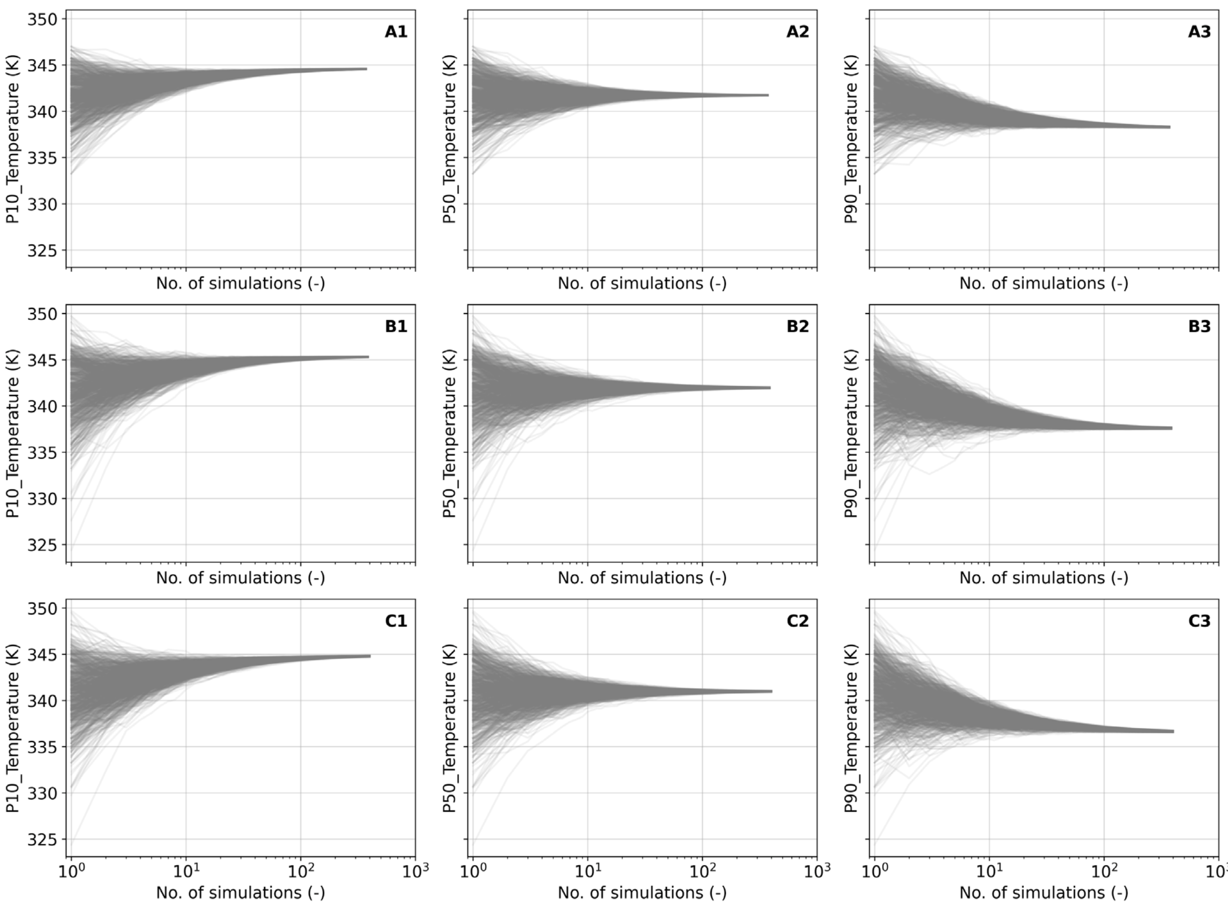

Fig. A3.1. Moving average of P10, P50 and P90 of production temperature after 50 years for the geological models created by different facies modeling approaches with an increasing number of simulations. A1 – A3 show the P10, P50 and P90 of the cases with three lithofacies constrained by GTD well data using OBM; B1 – B3 show the P10, P50 and P90 of the cases with three lithofacies constrained by GTD well data using SIS; C1 – C3 show the P10, P50 and P90 of the cases with three lithofacies not constrained by GTD well data using OBM.

energy demand of the campus and households and the economic performance, which is subject to changes when the thermal production starts. Fig. A2.1 shows that the produced energy is high at the beginning of the project. The energy demand from the geothermal project drops as time goes resulting in a decreasing in the injection rate. The average discharge rate is 3593.8 $m^3\,d^{-1}$ and the average injection temperature is 317.6 K.

A.3. Statistical convergence

The moving average of P10, P50 and P90 of production well BHT after 50 years versus the number of simulations, which are equivalent to the number of geological realizations, is evaluated to ensure the geological ensembles exhibit converged dynamic simulation results. As shown in Fig. A3.1, the expected values of P10, P50, and P90 exhibit minimal change after an ensemble of 400 simulations, which is similar to the finding in Major et al. (2023). In the case of the three-lithofacies models created by SIS, 20 out of 400 models failed in the dynamic simulation because of extremely low connectivity between the injection well and the production well.

Fig. A3.1 shows that the expected P10, P50 and P90 of production temperature have little change for the cases using either OBM or SIS that are constrained by the GTD well data (Fig. A3.1A1 – A3, Fig. A3.1B1 – B3). This hard constraint ensures a comparable result in the converged production temperature. The converged P10 of production well BHT is about 347.5 K for all three cases (Fig. A3.1A – C). However, there are 2.5 K to 3 K temperature differences in converged P50 and P90 of the production temperature comparing the cases of Fig. A3.1A – C. The difference in converged P50 and P90 of the production temperature shows the introduction of the GTD well data constrains the geological models.

Data availability

Data will be made available on request.

References

Aghaei, H., Colombera, L., Yan, N., Mountney, N.P., Bernagozzi, G., Di Giulio, A., 2024. Impact of fluvial meander-belt sedimentary heterogeneity on the efficiency of low-enthalpy geothermal doublets: Heat-transport simulations of forward stratigraphic models. Geoenergy 2 (1), http://dx.doi.org/10.1144/geoenergy2024-024, geoenergy2024–24.

Barnhoorn, A., Vondrak, A., Laumann, S., van Esser, B., Vargas Meleza, L., Abels, H.A., Vardon, P.J., 2024. Geothermal Project on TU Delft Campus - DEL-GT-01 and DEL-GT-02 Wireline Logs. 4TU.ResearchData, http://dx.doi.org/10.4121/2A7B2A63-DD7B-46BC-A275-97729B3AB348.V1.

Békési, E., Struijk, M., Bonté, D., Veldkamp, H., Limberger, J., Fokker, P.A., Vrijlandt, M., Van Wees, J.-D., 2020. An updated geothermal model of the Dutch subsurface based on inversion of temperature data. Geothermics 88, 101880. http://dx.doi.org/10.1016/j.geothermics.2020.101880.

Bradley, T., von Wilamowitz-Moellendorff, E., Laumann, S., Vardon, P.J., Barnhoorn, A., 2025. Quantifying porosity, permeability and reservoir quality in geothermal wells using a new high efficiency nuclear magnetic resonance logging methodology. In: European Geothermal Congress.

Bruhn, D., Abels, H.A., Barnhoorn, A., Bossennec, C., Braiden, A.K., Brehme, M., Chassagne, R., Daniilidis, A., Darnet, M., Drijkoningen, G., Fulton, P., Harcouët-Menou, V., Huenges, E., Jansen, S., Koulidis, A., Laumann, S., Lei, H., Moore, J., Rulff, P., Schöfisch, T., Slob, E., Vardon, P.J., Vargas-Meleza, L., Voskov, D., 2026. An urban energy laboratory for monitoring and better understanding of subsurface processes related to low-enthalpy geothermal heat production – UrbEnLab. Sci. Drill. 35 (1), 83–97. http://dx.doi.org/10.5194/sd-35-83-2026.

Bruhn, D.F., Wolf, K., Woning, M., Dalen, E.V., Nick, H.M., Willems, C.J.L., 2015. A research and production geothermal project on the TU Delft Campus: Project implementation and initial data collection. In: World Geotherm. Congr 2015. https://pangea.stanford.edu/ERE/db/WGC/papers/WGC/2015/35016.pdf.

Caers, J., 2005. Petroleum Geostatistics. Society of Petroleum EngineersRichardson, Texas, USA, http://dx.doi.org/10.2118/9781555631062.

Caumon, G., Collon-Drouaillet, P., Le Carlier de Veslud, C., Viseur, S., Sausse, J., 2009. Surface-based 3D modeling of geological structures. Math. Geosci. 41 (8), 927–945. http://dx.doi.org/10.1007/s11004-009-9244-2.

Chen, Y., Durlofsky, L.J., Gerritsen, M., Wen, X.H., 2003. A coupled local–global upscaling approach for simulating flow in highly heterogeneous formations. Adv. Water Resour. 26 (10), 1041–1060. http://dx.doi.org/10.1016/s0309-1708(03)00101-5.

Chen, Y., Rongier, G., Mullins, J.R., Voskov, D., Daniilidis, A., 2025a. Coupled numerical and analytical simulation on the delft campus geothermal well. In: Standford Geothermal Workshop 2025. https://pangea.stanford.edu/ERE/db/GeoConf/papers/SGW/2025/Chen1.pdf.

Chen, Y., Voskov, D., Daniilidis, A., 2025b. Rigorous numerical methodology and heat recovery analysis for modeling of direct use geothermal systems. Geoenergy Sci. Eng. 247, 213661. http://dx.doi.org/10.1016/j.geoen.2025.213661.

Chen, J., Zhao, Z., Wang, J., 2025. A time-series forecasting model-based optimization approach for well-doublet system in geothermal reservoirs under geological uncertainty. Energy 330, 136926. http://dx.doi.org/10.1016/j.energy.2025.136926.

Ciucci, M., 2023. Innovative technologies in the development of geothermal energy in Europe. https://www.europarl.europa.eu/RegData/etudes/BRIE/2023/754200/IPOL_BRI(2023)754200_EN.pdf.

Crooijmans, R.A., Willems, C.J.L., Nick, H.M., Bruhn, D.F., 2016. The influence of facies heterogeneity on the doublet performance in low-enthalpy geothermal sedimentary reservoirs. Geothermics 64, 209–219. http://dx.doi.org/10.1016/j.geothermics.2016.06.004.

Daniilidis, A., 2024. Towards comprehensive uncertainty quantification in direct-use geothermal systems. In: 85th EAGE Annual Conference & Exhibition (Including the Workshop Programme). European Association of Geoscientists & Engineers, pp. 1–5. http://dx.doi.org/10.3997/2214-4609.2024101678.

Daniilidis, A., Nick, H.M., Bruhn, D.F., 2020. Interdependencies between physical, design and operational parameters for direct use geothermal heat in faulted hydrothermal reservoirs. Geothermics 86, http://dx.doi.org/10.1016/j.geothermics.2020.101806.

Dejtrakulwong, P., Mukerji, T., Mavko, G., 2009. Investigating thomas-stieber model for property estimation of thin-bedded shaly-sand reservoirs. In: SEG Technical Program Expanded Abstracts 2009. Society of Exploration Geophysicists, pp. 1965–1969. http://dx.doi.org/10.1190/1.3255240.

Deutsch, C.V., Journel, A.G., 1998. GSLIB: Geostatistical Software Library and User's Guide, second ed. Oxford University Press, New York.

DHPC, D.H.P.C.C., 2024. DelftBlue supercomputer (Phase 2).

Donselaar, M.E., Gilding, D., Groenenberg, R., 2015. Reservoir geology and geothermal potential of the delft sandstone member in the west netherlands basin. In: World Geothermal Congress.

Dreyer, T., Fält, L.-M., 1993. Facies analysis and high-resolution sequence stratigraphy of the lower eocene shallow marine ametlla formation, Spanish Pyrenees. Sedimentology 40 (4), 667–697. http://dx.doi.org/10.1111/j.1365-3091.1993.tb01355.x.

Feyen, L., Caers, J., 2006. Quantifying geological uncertainty for flow and transport modeling in multi-modal heterogeneous formations. Adv. Water Resour. 29 (6), 912–929. http://dx.doi.org/10.1016/j.advwatres.2005.08.002.

Gershenzon, N., Ritzi, R., Dominic, D., Soltanian, M., Mehnert, E., Okwen, R., 2014. Influence of small-scale fluvial architecture on CO2 trapping processes in deep brine reservoirs. Water Resour. Res. 51, 8241–8256. http://dx.doi.org/10.1002/2015wr017638.

Gesbert, B., Geiger, S., Verschuur, E., Abels, H., Song, G., 2025. Insights from Integrated Geological and Seismic Modelling of Fluvial Geothermal Reservoirs, vol. 2025, (no. 1), pp. 1–5. http://dx.doi.org/10.3997/2214-4609.2025101348.

Gilding, D., 2010. Heterogeneity Determination of the Delft Subsurface for Heat Flow Modelling (Master thesis). Delft University of Technology.

Goovaerts, P., 1997. Geostatistics for Natural Resources Evaluation. Oxford University Press, http://dx.doi.org/10.1093/oso/9780195115383.001.0001.

Hadjisotiriou, G., Voskov, D., 2025. Machine learning assisted upscaling of compositional models. In: SPE Reservoir Simulation Conference. SPE, http://dx.doi.org/10.2118/223921-MS, D011S006R004.

Holden, L., Hauge, R., Skare, Ø., Skorstad, A., 1998. Modeling of fluvial reservoirs with object models. Math. Geol. 30 (5), 473–496. http://dx.doi.org/10.1023/A:1021769526425.

Journal, A., Alabert, F., 1989. Non-gaussian data expansion in the earth sciences. Terra Nova 1 (2), 123–134. http://dx.doi.org/10.1111/j.1365-3121.1989.tb00344.x.

Journel, A.G., 1983. Nonparametric estimation of spatial distributions. J. Int. Assoc. Math. Geol. 15 (3), 445–468. http://dx.doi.org/10.1007/BF01031292.

Khait, M., Voskov, D., 2017. GPU-offloaded general purpose simulator for multiphase flow in porous media. In: SPE Reservoir Simulation Conference. SPE, http://dx.doi.org/10.2118/182663-MS.

Khait, M., Voskov, D., 2018a. Adaptive parameterization for solving of thermal/compositional nonlinear flow and transport with buoyancy. SPE J. 23 (2), 522–534. http://dx.doi.org/10.2118/182685-PA.

Khait, M., Voskov, D., 2018b. Operator-based linearization for efficient modeling of geothermal processes. Geothermics 74, 7–18. http://dx.doi.org/10.1016/j.geothermics.2018.01.012.

Khait, M., Voskov, D., 2019. Integrated framework for modelling of thermal-compositional multiphase flow in porous media. In: SPE Reservoir Simulation Conference. SPE, http://dx.doi.org/10.2118/193932-MS.

Larue, D.K., Hovadik, J., 2006. Connectivity of channelized reservoirs: A modelling approach. Pet. Geosci. 12 (4), 291–308. http://dx.doi.org/10.1144/1354-079306-699.

Liotta, D., Brogi, A., Ruggieri, G., Zucchi, M., 2021. Fossil vs. Active geothermal systems: A field and laboratory method to disclose the relationships between geothermal fluid flow and geological structures at depth. Energies 14, 933. http://dx.doi.org/10.3390/en14040933.

Liu, G., Pu, H., Zhao, Z., Liu, Y., 2019. Coupled thermo-hydro-mechanical modeling on well pairs in heterogeneous porous geothermal reservoirs. Energy 171, 631–653. http://dx.doi.org/10.1016/j.energy.2019.01.022.

Lund, J.W., Toth, A.N., 2021. Direct utilization of geothermal energy 2020 worldwide review. Geothermics 90, 101915, ISBN: 0375-6505 Publisher: Elsevier.

Major, M., Daniilidis, A., Hansen, T.M., Khait, M., Voskov, D., 2023. Influence of process-based, stochastic and deterministic methods for representing heterogeneity in fluvial geothermal systems. Geothermics 109, http://dx.doi.org/10.1016/j.geothermics.2023.102651.

Matheron, G., 1973. The intrinsic random functions and their applications. Adv. in Appl. Probab. 5 (3), 439–468. http://dx.doi.org/10.2307/1425829.

Mijnlieff, H.F., 2020. Introduction to the geothermal play and reservoir geology of the netherlands. Neth. J. Geosci. 99, http://dx.doi.org/10.1017/njg.2020.2.

Mijnlieff, H., Ramsak, P., Lako, P., 2013. Geothermal energy and support schemes in the netherlands. In: European Geothermal Congress. pp. 1–8.

Mo, S., Shi, X., Lu, D., Ye, M., Wu, J., 2019. An adaptive kriging surrogate method for efficient uncertainty quantification with an application to geological carbon sequestration modeling. Comput. Geosci. 125, 69–77. http://dx.doi.org/10.1016/j.cageo.2019.01.012.

Mottaghy, D., Pechnig, R., Vogt, C., 2011. The geothermal project den haag: 3D numerical models for temperature prediction and reservoir simulation. Geothermics 40 (3), 199–210. http://dx.doi.org/10.1016/j.geothermics.2011.07.001.

Park, J., Yang, G., Satija, A., Scheidt, C., Caers, J., 2016. DGSA: A Matlab toolbox for distance-based generalized sensitivity analysis of geoscientific computer experiments. Comput. Geosci. 97, 15–29. http://dx.doi.org/10.1016/j.cageo.2016.08.021.

Perkins, D., 2019. Reservoir Simulation for Play-based Development of Low Enthalpy Geothermal Resources: Application to the Delft Sandstone (Master thesis). Delft University of Technology.

Perzan, Z., 2025. pyDGSA: v1.0.8. Zenodo, http://dx.doi.org/10.5281/zenodo.15558057.

Platform Geothermie, DAGO, Wartenetwerk, EBN, 2018. Master plan geothermal energy in the netherlands. https://geothermie.nl/images/bestanden/Masterplan_Aardwarmte_in_Nederland_ENG.pdf.

Prud'homme, C., Rovas, D.V., Veroy, K., Machiels, L., Maday, Y., Patera, A.T., Turinici, G., 2002. Reliable real-time solution of parametrized partial differential equations: Reduced-basis output bound methods. J. Fluids Eng. 124 (1), 70–80. http://dx.doi.org/10.1115/1.1448332.

Pruess, K., Oldenburg, C., Moridis, G., 1999. Tough2 User's Guide. Technical Report, Lawrence Berkeley National Laboratory, http://tough.lbl.gov/assets/docs/TOUGH2_V2_Users_Guide.pdf.

Qin, Z., Jiang, A., Faulder, D., Cladouhos, T.T., Jafarpour, B., 2024. Physics-guided deep learning for prediction of energy production from geothermal reservoirs. Geothermics 116, 102824. http://dx.doi.org/10.1016/j.geothermics.2023.102824.

Reinhard, P., 2019. Pressure and Temperature Interference for Geothermal Projects in Dense Production Areas A Case Study for the Delft Area. (Master's Thesis). Delft University of Technology.

Ringrose, P., 2014. Reservoir Model Design: a Practitioner's Guide. Springer.

Scheidt, C., Caers, J., 2009. Representing spatial uncertainty using distances and kernels. Math. Geosci. 41 (4), 397–419. http://dx.doi.org/10.1007/s11004-008-9186-0.

SodM, TNO, 2013. Protocol_injectiedrukken_bij_aardwarmte.

Stieber, S., 1970. Pulsed neutron capture log evaluation - Louisiana Gulf Coast. In: Fall Meeting of the Society of Petroleum Engineers of AIME. SPE, pp. SPE–2961–MS. http://dx.doi.org/10.2118/2961-MS.

Tiab, D., Donaldson, E.C., 2016. Porosity and permeability. In: Petrophysics. Elsevier, pp. 67–186.

TNO, 1977. Dutch oil and gas portal. https://www.nlog.nl/.

Ullah, J., Li, H., Förster, H.J., Abdalla, R.M., Ehsan, M., Faisal, M., 2024. Harvesting Earth's heat: A deep learning Odyssey for reservoir characterization and sustainable geothermal energy management. Geoenergy Sci. Eng. 238, 212921. http://dx.doi.org/10.1016/j.geoen.2024.212921.

Vardon, P., Abels, H., Barnhoorn, A., Daniilidis, A., Bruhn, D., Drijkoningen, G., Elliott, K., van Esser, B., Laumann, S., van Paassen, P., Vargas Meleza, L., Vondrak, A., Voskov, D., 2024. A research and production geothermal project on the TU Delft Campus: Project implementation and initial data collection. In: Standford Geothermal Workshop 2024. pp. 1–7, https://pangea.stanford.edu/ERE/db/GeoConf/papers/SGW/2024/Vardon.pdf.

Verweij, J., Simmelink, H., Underschultz, J., Witmans, N., 2014. Pressure and fluid dynamic characterisation of the Dutch subsurface. Neth. J. Geosci. - Geol. En Mijnb. 91 (4), 465–490. http://dx.doi.org/10.1017/S0016774600000342.

Vogt, C., Mottaghy, D., Wolf, A., Rath, V., Pechnig, R., Clauser, C., 2010. Reducing temperature uncertainties by stochastic geothermal reservoir modelling. Geophys. J. Int. 181 (1), 321–333. http://dx.doi.org/10.1111/j.1365-246X.2009.04498.x.

Voskov, D.V., 2017. Operator-based linearization approach for modeling of multiphase multi-component flow in porous media. J. Comput. Phys. 337, 275–288. http://dx.doi.org/10.1016/j.jcp.2017.02.041.

Voskov, D., Abels, H., Barnhoorn, A., Chen, Y., Daniilidis, A., Drijkoningen, G., Geiger, S., Laumann, S., Song, G., Vardon, P.J., Meleza, L.V., Verschuur, E., Vondrak, A., 2024a. A research and production geothermal project on the TU Delft campus: initial modeling and establishment of a digital twin. In: Standford Geothermal Workshop 2024. https://pangea.stanford.edu/ERE/db/GeoConf/papers/SGW/2024/Voskov.pdf.

Voskov, D., Saifullin, I., Novikov, A., Wapperom, M., Orozco, L., Seabra, G.S., Chen, Y., Khait, M., Lyu, X., Tian, X., De Hoop, S., Palha, A., 2024b. open Delft Advanced Research Terra Simulator(open-DARTS). J. Open Source Softw. 9 (99), 6737. http://dx.doi.org/10.21105/joss.06737.

Voskov, D., Zhou, Y., 2015. AD-GPRS, Stanford University's Automatic Differentiation based General Purpose Research Simulator User's Manual. Technical Report, Stanford University, http://pangea.stanford.edu/researchgroups/supri-b/.

Wang, Y., Voskov, D., Daniilidis, A., Khait, M., Saeid, S., Bruhn, D., 2023. Uncertainty quantification in a heterogeneous fluvial sandstone reservoir using GPU-based Monte Carlo simulation. Geothermics 114, 102773. http://dx.doi.org/10.1016/j.geothermics.2023.102773.

Wang, Y., Voskov, D., Khait, M., Bruhn, D., 2020. An efficient numerical simulator for geothermal simulation: A benchmark study. Appl. Energy 264, 114693. http://dx.doi.org/10.1016/j.apenergy.2020.114693.

Wang, Y., Voskov, D., Khait, M., Saeid, S., Bruhn, D., 2021. Influential factors on the development of a low-enthalpy geothermal reservoir: A sensitivity study of a realistic field. Renew. Energy 179, 641–651. http://dx.doi.org/10.1016/j.renene.2021.07.017.

Watanabe, N., Wang, W., McDermott, C.I., Taniguchi, T., Kolditz, O., 2010. Uncertainty analysis of thermo-hydro-mechanical coupled processes in heterogeneous porous media. Comput. Mech. 45 (4), 263–280. http://dx.doi.org/10.1007/s00466-009-0445-9.

Wellmann, J.F., Horowitz, F.G., Schill, E., Regenauer-Lieb, K., 2010. Towards incorporating uncertainty of structural data in 3D geological inversion. Tectonophysics 490 (3), 141–151. http://dx.doi.org/10.1016/j.tecto.2010.04.022.

Wiggers, C.J.I., 2009. The Delft Sandstone in the West Netherlands Basin (Bachelor thesis). Delft University of Technology.

Willems, C., 2012. Study of the Lower Cretaceous Sands in the Van Den Bosch Geothermal Energy Concession (Master thesis). Delft University of Technology.

Willems, C.J.L., Nick, H.M., Donselaar, M.E., Weltje, G.J., Bruhn, D.F., 2017. On the connectivity anisotropy in fluvial Hot Sedimentary Aquifers and its influence on geothermal doublet performance. Geothermics 65, 222–233. http://dx.doi.org/10.1016/j.geothermics.2016.10.002.

Willems, C.J., Vondrak, A., Mijnlieff, H.F., Donselaar, M.E., Van Kempen, B.M., 2020. Geology of the Upper Jurassic to Lower Cretaceous geothermal aquifers in the West Netherlands Basin – an overview. Neth. J. Geosci. 99, e1. http://dx.doi.org/10.1017/njg.2020.1.

Willems, C.J., Vondrak, A., Munsterman, D.K., Donselaar, M.E., Mijnlieff, H.F., 2017. Regional geothermal aquifer architecture of the fluvial lower cretaceous nieuwerkerk formation – a palynological analysis. Neth. J. Geosci. 96 (4), 319–330. http://dx.doi.org/10.1017/njg.2017.23.

Willis, B.J., Tang, H., 2010. Three-dimensional connectivity of point-bar deposits. J. Sediment. Res. 80 (5), 441–454. http://dx.doi.org/10.2110/jsr.2010.046.

Wong, Z., Horne, R., Voskov, D., 2015. A geothermal reservoir simulator in AD-GPRS. In: World Geothermal Congress. https://pangea.stanford.edu/ERE/db/WGC/papers/WGC/2015/22043.pdf.

Zhang, L., Daniilidis, A., Dieudonné, A.-C., Thibaut, R., Hermans, T., 2026. A bayesian evidential learning framework for safety and performance prediction in thermo-hydro-mechanical coupled deep mine geothermal systems. J. Rock Mech. Geotech. Eng. http://dx.doi.org/10.1016/j.jrmge.2025.11.022.

Zhang, L., Dieudonné, A.-C., Daniilidis, A., Dong, L., Cao, W., Thibaut, R., Tas, L., Hermans, T., 2025. Thermo-hydro-mechanical modeling of geothermal energy systems in deep mines: Uncertainty quantification and design optimization. Appl. Energy 377, 124531. http://dx.doi.org/10.1016/j.apenergy.2024.124531.

Zhou, Q., Yang, X., Zhang, R., Hosseini, S., Ajo-Franklin, J., Freifeld, B., Daley, T., Hovorka, S., 2020. Dynamic processes of CO2 storage in the field: 1. Multiscale and multipath channeling of CO2 flow in the hierarchical fluvial reservoir at cranfield, mississippi. Water Resour. Res. 56.